PHYSICAL REVIEW B **109**, 085436 (2024)

Momentum mismatch driven bound states in the continuum and ellipsometric phase singularities

Feng Wu[1,*] Xin Qi,[2] Meibao Qin,[3] Ma Luo,[1] Yang Long,[4] Jiaju Wu,[2] Yong Sun,[2] Haitao Jiang,[2,†]
Tingting Liu,[5,6] Shuyuan Xiao,[5,6,‡] and Hong Chen[2]
[1]*School of Optoelectronic Engineering, Guangdong Polytechnic Normal University, Guangzhou 510665, China*
[2]*MOE Key Laboratory of Advanced Micro-Structured Materials, School of Physics Science and Engineering, Tongji University, Shanghai 200092, China*
[3]*School of Education, Nanchang Institute of Science and Technology, Nanchang 330108, China*
[4]*Division of Physics and Applied Physics, School of Physical and Mathematical Sciences, Nanyang Technological University, Singapore 637371, Singapore*
[5]*Institute for Advanced Study, Nanchang University, Nanchang 330031, China*
[6]*Jiangxi Key Laboratory for Microscale Interdisciplinary Study, Nanchang University, Nanchang 330031, China*

(Received 14 December 2023; revised 13 February 2024; accepted 13 February 2024; published 29 February 2024)

In this paper, we elucidate the formation of bound states in the continuum (BICs) in compound grating waveguide structures from the perspective of momentum mismatch. As the complex lattice reduces to a simple lattice, the excitable guided resonance turns into an unexcitable BIC due to momentum mismatch. Herein, we refer to this state as momentum mismatch driven BIC. Interestingly, as the incidence changes from normal to oblique, the single momentum mismatch driven BIC splits into dual momentum mismatch driven BICs due to the nonzero tangential momentum of the incident light. Distinct from conventional symmetry-protected and accidental BICs, momentum mismatch driven BICs lie in sections of photonic bands. Consequently, Q factors of momentum mismatch driven quasi-BICs exhibit angular robustness far beyond conventional symmetry-protected and accidental quasi-BICs. Empowered by the momentum mismatch driven BIC, a pair of ellipsometric phase singularities emerge. Enabled by the drastic ellipsometric phase change, ultrasensitive refractive index sensing can be achieved. These results not only provide unique insights into the relation between momentum, BICs, and ellipsometric phase, but also offer a recipe for developing high-performance phase-based optical devices, such as ultrasensitive sensors, wave plates, and spatial light modulators.

DOI: 10.1103/PhysRevB.109.085436

I. INTRODUCTION

Bound states in the continuum (BICs)—localized states embedded inside continuous spectra—provide unique insights into nanophotonics [1–3]. After introducing perturbations, BICs with infinitely high quality (Q) factors turn into quasi-BICs with finitely high Q factors [4–7]. Owing to their ultrastrong resonant properties, quasi-BICs have been extensively exploited in low-threshold lasing [8–11], ultrasensitive sensing [12–19], strong chirality [20–26], polarization manipulation [27–30], unidirectional transport [31–33], high-efficiency harmonic generation [34–37], and enhancement of light absorption [38,39]. In the past two decades, two classes of BICs, symmetry-protected [4,40] and accidental BICs [41,42], have attracted considerable attention. Symmetry-protected BICs located at the Γ point in the first Brillouin zone are protected by the in-plane inversion symmetry of structures [4,40]. Symmetry-protected BICs turn into quasi-BICs when deviating from the Γ point. Accidental BICs located at off-Γ or Γ points originate from the destructive interference between two radiation channels [41,42]. Similarly, accidental BICs turn into quasi-BICs when an in-plane wave vector is changed. Therefore, conventional symmetry-protected and accidental quasi-BICs can only maintain ultrahigh Q factors in ultranarrow angle ranges.

Interestingly, researchers discovered a category of special BICs in subwavelength gratings [43–63] and metasurfaces with complex lattices [64–76]. Recently, the formation mechanisms of this category of BICs have attracted great interest [48–63,68–76]. In 2018, Overvig *et al.* discussed this category of BICs from the perspective of band folding in subwavelength gratings [48]. Such perspective has been further developed in subwavelength gratings [49–54] and extended to metasurfaces [68–76]. In 2019, we discussed this category of BICs from the perspective of guided-mode resonance in subwavelength gratings [55]. Such perspective has also been further developed in subwavelength gratings [56–63]. In this paper, we elucidate the formation of this category of BICs from the perspective of momentum mismatch in compound grating waveguide structures and herein referred to as recently discovered momentum mismatch driven BICs. When the lattice of the compound grating waveguide structure changes from complex to simple, the excitable guided resonance evolves into an unexcitable BIC due to momentum

---

[*] fengwu@gpnu.edu.cn
[†] jiang-haitao@tongji.edu.cn
[‡] syxiao@ncu.edu.cn

2469-9950/2024/109(8)/085436(16)

mismatch. In addition, we establish a bridge connecting the perspectives of band folding and guided-mode resonance. More importantly, we disclose two exotic properties of momentum mismatch driven BICs. As the incidence changes from normal to oblique, the single momentum mismatch driven BIC splits into dual momentum mismatch driven BICs due to the nonzero tangential momentum of the incident light. In addition, distinct from conventional symmetry-protected [4,40] and accidental quasi-BICs [41,42], momentum mismatch driven quasi-BICs maintain ultrahigh Q factors over much broader angle ranges. It should be noted that momentum mismatch driven BICs in this work are different from the recently discovered Brillouin zone folding driven BICs in metasurfaces with complex lattices [77]. The mechanism of the formation of Brillouin- zone folding driven BICs can be explained as follows. When the lattice of the metasuface changes from simple to complex, the first Brillouin zone halves. Hence, the modes previously located at the edge of the first Brillouin zone are folded into the Γ point. Among these folded modes, the folded modes whose symmetries do not match the symmetry of a radiative plane wave are called Brillouin zone folding driven BICs [77]. In other words, Brillouin zone folding driven BICs are located at the Γ point. Similar to conventional symmetry-protected BICs, Brillouin zone folding driven BICs turn into quasi-BICs when deviating from the Γ point. Empowered by the Brillouin zone folding, Q factors of Brillouin zone folding driven quasi-BICs exhibit superior robustness against the structural disorders [77].

As a fundamental property of light, phase plays a vital role in orbital angular momentum [78,79], biosensing [80], perfect absorption [81,82], and polarization manipulation [83,84]. The ellipsometric phase refers to the reflection phase difference between transverse magnetic (TM) and transverse electric (TE) polarizations [85,86]. Recently, researchers achieved ellipsometric phase singularities based on Fabry-Perot resonances [87,88], Tamm plasmon polaritons [89–93], and Bloch surface waves [94,95]. Nonetheless, the relation between ellipsometric phase and BICs has not yet been studied. In this paper, we elucidate the relation between ellipsometric phase and momentum mismatch driven BICs. Empowered by a momentum mismatch driven BIC, a pair of ellipsometric phase singularities emerge. Since the momentum mismatch driven quasi-BIC maintains an ultrahigh Q factor over a broad angle range, the drastic ellipsometric phase change demonstrates a superior robustness against the incident angle. Enabled by a drastic ellipsometric phase change, ultrasensitive refractive index sensing can be achieved. The minimum resolution reaches the order of 10^{-8} RIU (refractive index unit). Our findings not only provide unique insights into the relation between momentum, BICs, and ellipsometric phase, but also offer a recipe for developing high-performance phase-based optical devices.

This paper is organized as follows. In Sec. II, we demonstrate the physical mechanism of momentum mismatch driven BICs in compound grating waveguide structures. Then, we discuss the robustness of the Q factor of the momentum mismatch driven quasi-BIC against the incident angle. In Sec. III, we realize a pair of ellipsometric phase singularities empowered by the momentum mismatch driven BIC. In Sec. IV, as an example of the applications, we achieve ultrasensitive refractive index sensing enabled by a drastic ellipsometric phase change. Finally, the conclusions are presented in Sec. V.

II. MOMENTUM MISMATCH DRIVEN BIC IN COMPOUND GRATING WAVEGUIDE STRUCTURE

This section is organized as follows. In Secs. II A and II B, we demonstrate the physical mechanism of the momentum mismatch driven BIC in the compound grating waveguide structure at normal and oblique incidences, respectively. When the incidence changes from normal to oblique, the single momentum mismatch driven BIC splits into dual momentum mismatch driven BICs due to the nonzero tangential momentum of the incident light. In Sec. II C, we discuss the robustness of the Q factor of the momentum mismatch driven quasi-BIC against the incident angle.

A. Physical mechanism of momentum mismatch driven BIC in compound grating waveguide structure at normal incidence

Figures 1(a) and 1(b) schematically depict the unit cells of the compound grating waveguide structures for the unperturbed and perturbed cases, respectively. The insets show the corresponding first Brillouin zones. The compound grating waveguide structure consists of a subwavelength hafnium dioxide (HfO_2) grating layer, a HfO_2 waveguide layer, and a silica (SiO_2) substrate layer. The refractive indices of HfO_2 and SiO_2 are set as $n_H = n_{WG} = 1.88$ [96] and $n_S = 1.44$ [97], respectively. The heights of the subwavelength HfO_2 grating and waveguide layers are denoted by h_G and h_{WG}, respectively. The width of the HfO_2 ridge in the grating layer is denoted by w_H. For the unperturbed case, the widths of two adjacent air grooves in the grating layer are set to be the same, i.e., $w_{L1} = w_{L2}$. Therefore, the period of the grating layer is $p = w_H + w_{L1}$. For the perturbed case, the widths of two adjacent air grooves in the grating layer are set to be different, i.e., $w_{L1} \neq w_{L2}$. The perturbations are applied to each unit cell. Distinct from the unperturbed case, the period of the grating layer doubles, i.e., $p' = 2p$. Consequently, the first Brillouin zone is reduced by half. Suppose that a linearly polarized plane wave perpendicularly launches onto the structure in the xOz plane. Starting from the guided-mode resonance (GMR) theory, we demonstrate that the unperturbed structure supports momentum mismatch driven BICs, whereas the perturbed structure supports momentum mismatch driven quasi-BICs. The geometric parameters are selected as $h_G = 120$ nm, $h_{WG} = 340$ nm, $p = 427.5$ nm, and $w_H = f_H p = 0.6p$.

According to the GMR theory, the momentum-matching condition for the unperturbed structure can be expressed as [98]

$$k_{x,m} = -m\frac{2\pi}{p} = \beta \quad (m = \pm 1, \pm 2, \ldots), \tag{1}$$

where m denotes the diffraction order, $2\pi/p$ denotes the basic momentum provided by the grating layer, and β denotes the tangential momentum of the guided mode.

Throughout this work, we focus on the fundamental guided modes for TM and TE polarizations, i.e., TM_0 and TE_0 guided modes. According to the four-layer slab waveguide model, the

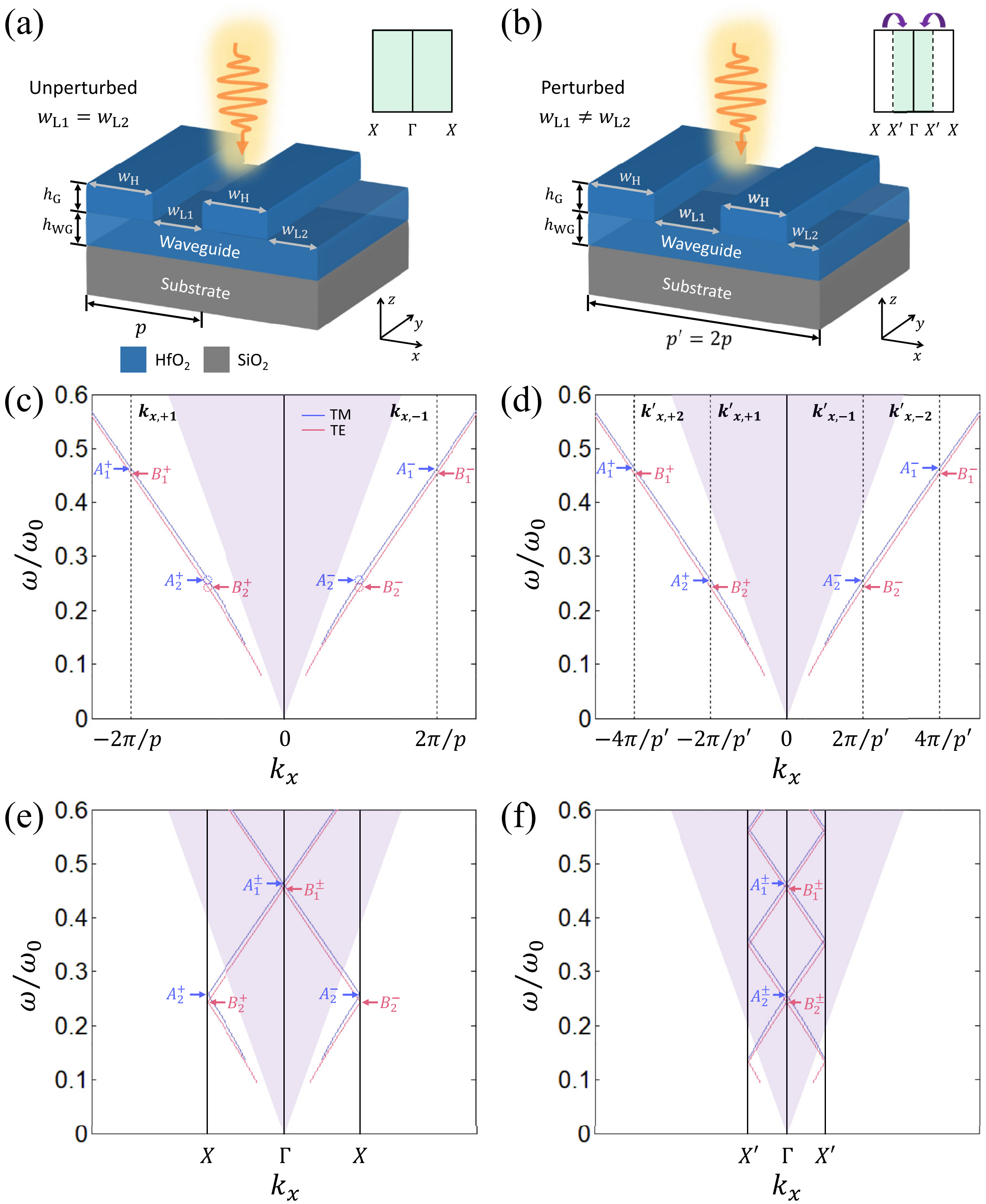

FIG. 1. Schematics of the unit cells of the compound grating waveguide structures for (a) unperturbed and (b) perturbed cases. The insets show the corresponding first Brillouin zones. Momentum-frequency relations in infinite momentum spaces for (c) unperturbed and (d) perturbed cases. The purple-shadowed region represents the light cone. Momentum-frequency relations folded into the first Brillouin zones for (e) unperturbed and (f) perturbed cases.

momentum-frequency relation for TM$_0$ guided mode $\beta_{\mathrm{TM}_0}(\omega)$ takes the following form [58,98,99]:

$$h_{\mathrm{WG}}\sqrt{k_0^2 n_{\mathrm{WG}}^2 - \beta_{\mathrm{TM}_0}^2} = \arctan\left(\frac{n_{\mathrm{WG}}^2\sqrt{\beta_{\mathrm{TM}_0}^2 - k_0^2 n_{\mathrm{S}}^2}}{n_{\mathrm{S}}^2\sqrt{k_0^2 n_{\mathrm{WG}}^2 - \beta_{\mathrm{TM}_0}^2}}\right) + \arctan\left(\kappa_{\mathrm{TM}_0}\frac{n_{\mathrm{WG}}^2\sqrt{\beta_{\mathrm{TM}_0}^2 - k_0^2 n_{\mathrm{eff}}^2}}{n_{\mathrm{eff}}^2\sqrt{k_0^2 n_{\mathrm{WG}}^2 - \beta_{\mathrm{TM}_0}^2}}\right), \tag{2}$$

where

$$\kappa_{\mathrm{TM_0}} = \tanh\left[\operatorname{arctanh}\left(\frac{n_{\mathrm{eff}}^2\sqrt{\beta_{\mathrm{TM_0}}^2 - k_0^2 n_0^2}}{n_0^2\sqrt{\beta_{\mathrm{TM_0}}^2 - k_0^2 n_{\mathrm{eff}}^2}}\right) + h_{\mathrm{G}}\sqrt{\beta_{\mathrm{TM_0}}^2 - k_0^2 n_{\mathrm{eff}}^2}\right]. \quad (3)$$

Similarly, the momentum-frequency relation for $\mathrm{TE_0}$ guided mode $\beta_{\mathrm{TE_0}}(\omega)$ takes the following form [58,98,99]:

$$h_{\mathrm{WG}}\sqrt{k_0^2 n_{\mathrm{WG}}^2 - \beta_{\mathrm{TE_0}}^2} = \arctan\left(\frac{\sqrt{\beta_{\mathrm{TE_0}}^2 - k_0^2 n_{\mathrm{S}}^2}}{\sqrt{k_0^2 n_{\mathrm{WG}}^2 - \beta_{\mathrm{TE_0}}^2}}\right) + \arctan\left(\kappa_{\mathrm{TE_0}}\frac{\sqrt{\beta_{\mathrm{TE_0}}^2 - k_0^2 n_{\mathrm{eff}}^2}}{\sqrt{k_0^2 n_{\mathrm{WG}}^2 - \beta_{\mathrm{TE_0}}^2}}\right), \quad (4)$$

where

$$\kappa_{\mathrm{TE_0}} = \tanh\left[\operatorname{arctanh}\left(\frac{\sqrt{\beta_{\mathrm{TE_0}}^2 - k_0^2 n_0^2}}{\sqrt{\beta_{\mathrm{TE_0}}^2 - k_0^2 n_{\mathrm{eff}}^2}}\right) + h_{\mathrm{G}}\sqrt{\beta_{\mathrm{TE_0}}^2 - k_0^2 n_{\mathrm{eff}}^2}\right]. \quad (5)$$

In Eqs. (2)-(5), $n_{\mathrm{eff}} = f_{\mathrm{H}} n_{\mathrm{H}} + (1 - f_{\mathrm{H}}) n_{\mathrm{L}} = 1.528$ represents the effective refractive index of the grating layer. According to Eqs. (2)-(5), we calculate the momentum-frequency relations for the $\mathrm{TM_0}$ and $\mathrm{TE_0}$ guided modes, as shown by the blue and red solid lines in Fig. 1(c), respectively. The normalized angular frequency is $\omega_0 = 2\pi c/h_{\mathrm{WG}}$. The purple-shadowed region represents the light cone. As demonstrated, the momentum-frequency relations for the $\mathrm{TM_0}$ and $\mathrm{TE_0}$ guided modes lie below the light cone. Owing to momentum mismatch, the incident light cannot couple with the guided mode without the grating layer. The cutoff angular frequencies for the $\mathrm{TM_0}$ and $\mathrm{TE_0}$ guided modes are $\omega_{\mathrm{c,TM_0}} = 0.1370\omega_0$ and $\omega_{\mathrm{c,TE_0}} = 0.0797\omega_0$, respectively. According to Eq. (1), we plot the momentum-frequency relations $k_{x,\pm1}$, as shown by the black dashed lines in Fig. 1(c). For TM polarization, two momentum-matching points (marked by $A_1^{\pm}$) occur at the same angular frequency $\omega_{\pm1}^{\mathrm{TM}} = 0.4632\omega_0$ ($\lambda_{\pm1}^{\mathrm{TM}} = 734.0$ nm), giving rise to a Fano resonance. For TE polarization, two momentum-matching points (marked by $B_1^{\pm}$) occur at the same angular frequency $\omega_{\pm1}^{\mathrm{TE}} = 0.4534\omega_0$ ($\lambda_{\pm1}^{\mathrm{TE}} = 749.9$ nm), also giving rise to a Fano resonance.

For the perturbed structure, the period of the grating layer doubles. Consequently, the momentum-matching condition becomes

$$k'_{x,m'} = -m'\frac{2\pi}{p'} = -m'\frac{\pi}{p} = \beta \quad (m' = \pm1, \pm2, \ldots). \quad (6)$$

The basic momentum provided by the grating layer is reduced by half, i.e., $2\pi/p' = \pi/p$. Interestingly, the momentum-frequency relations $k'_{x,\pm2m}$ overlap with the momentum-frequency relations $k_{x,\pm m}$. According to Eq. (6), we plot the momentum-frequency relations $k'_{x,\pm1}$ and $k'_{x,\pm2}$, as shown by the black dashed lines in Fig. 1(d). For TM polarization, four momentum-matching points (marked by $A_1^{\pm}$ and $A_2^{\pm}$) occur at two angular frequencies $\omega_{\pm1}^{\mathrm{TM}} = 0.4632\omega_0$ ($\lambda_{\pm1}^{\mathrm{TM}} = 734.0$ nm) and $\omega_{\pm2}^{\mathrm{TM}} = 0.2571\omega_0$ ($\lambda_{\pm2}^{\mathrm{TM}} = 1322.4$ nm), giving rise to two Fano resonances. For TE polarization, four momentum-matching points (marked by $B_1^{\pm}$ and $B_2^{\pm}$) occur at two angular frequencies $\omega_{\pm1}^{\mathrm{TE}} = 0.4534\omega_0$ ($\lambda_{\pm1}^{\mathrm{TE}} = 749.9$ nm) and $\omega_{\pm2}^{\mathrm{TE}} = 0.2439\omega_0$ ($\lambda_{\pm2}^{\mathrm{TE}} = 1394.0$ nm), also giving rise to two Fano resonances.

We define a perturbation parameter as $\alpha = (w_{\mathrm{L1}} - w_{\mathrm{L2}})/(w_{\mathrm{L1}} + w_{\mathrm{L2}})$. Considering a parameter changing process $\alpha \neq 0 \rightarrow \alpha = 0$, the perturbed structure turns into an unperturbed structure. Consequently, the previously excitable guided resonances at angular frequencies $\omega_{\pm2}^{\mathrm{TM}} = 0.2571\omega_0$ ($\lambda_{\pm2}^{\mathrm{TM}} = 1322.4$ nm) and $\omega_{\pm2}^{\mathrm{TE}} = 0.2439\omega_0$ ($\lambda_{\pm2}^{\mathrm{TE}} = 1394.0$ nm) become unexcitable since the momentum-matching conditions are broken. Hence, these dark modes can be called momentum mismatch driven BICs.

Next, we demonstrate the equivalence of momentum mismatch driven BICs and BICs induced by band folding [48–54]. Owing to the periodicity of the grating layer, the infinite momentum space is folded into the first Brillouin zone. Now, we fold the momentum-frequency relations of the $\mathrm{TM_0}$ and $\mathrm{TE_0}$ guided modes into the first Brillouin zone for the unperturbed and perturbed cases, as shown in Figs. 1(e) and 1(f), respectively. This method is also known as the *empty-lattice approximation* [100,101]. It should be noted that the empty-lattice approximation is valid since the thickness of the grating layer is only $h_{\mathrm{G}} = 120$ nm. The validation of the empty-lattice approximation is further confirmed by the reflectance spectra in Figs. 2(a) and 2(c). For the unperturbed structure, the edges of the first Brillouin zone are located at $k_x = \pm\pi/p$. Since we consider normal incidence, only the modes in the momentum-frequency relations of the $\mathrm{TM_0}$ and $\mathrm{TE_0}$ guided modes at the Γ point can be excited by the incident light. Comparing Fig. 1(e) with 1(c), we can conclude that these excitable modes in Fig. 1(e) are identical with modes $A_1^{\pm}$ and $B_1^{\pm}$ in Fig. 1(c). Owing to the periodicity, modes $A_1^{\pm}$ and $B_1^{\pm}$ are folded into the Γ point. In addition, dark modes $A_2^{\pm}$ and $B_2^{\pm}$ are located at the edges of the first Brillouin zone. These modes cannot be excited by the incident light since they lie below the light cone. For the perturbed structure, the edges of the first Brillouin zone are located at $k_x = \pm\pi/p' = \pm\pi/2p$. Hence, the first Brillouin zone is reduced by half. Comparing Fig. 1(f) with 1(d), we can conclude that the excitable modes in Fig. 1(f) are identical with modes $A_1^{\pm}$, $B_1^{\pm}$, $A_2^{\pm}$, and $B_2^{\pm}$ in Fig. 1(d). Owing to the periodicity, modes $A_1^{\pm}$, $B_1^{\pm}$, $A_2^{\pm}$, and $B_2^{\pm}$ are folded into the Γ point. Considering the parameter changing process $\alpha = 0 \rightarrow \alpha \neq 0$, the momentum mismatch driven BICs previously located at the edges of the first Brillouin zone turn into momentum mismatch driven quasi-BICs located at the Γ point inside the light cone, which is consistent with the results in Refs. [48–54]. Before introducing perturbation, modes $A_2^{\pm}$ and $B_2^{\pm}$ lie below the light cone. However, after introducing infinitely weak perturbation, modes $A_2^{\pm}$ and $B_2^{\pm}$ are folded into the Γ point.

To further confirm the formation of the momentum mismatch driven BIC, we utilize the rigorous coupled-wave

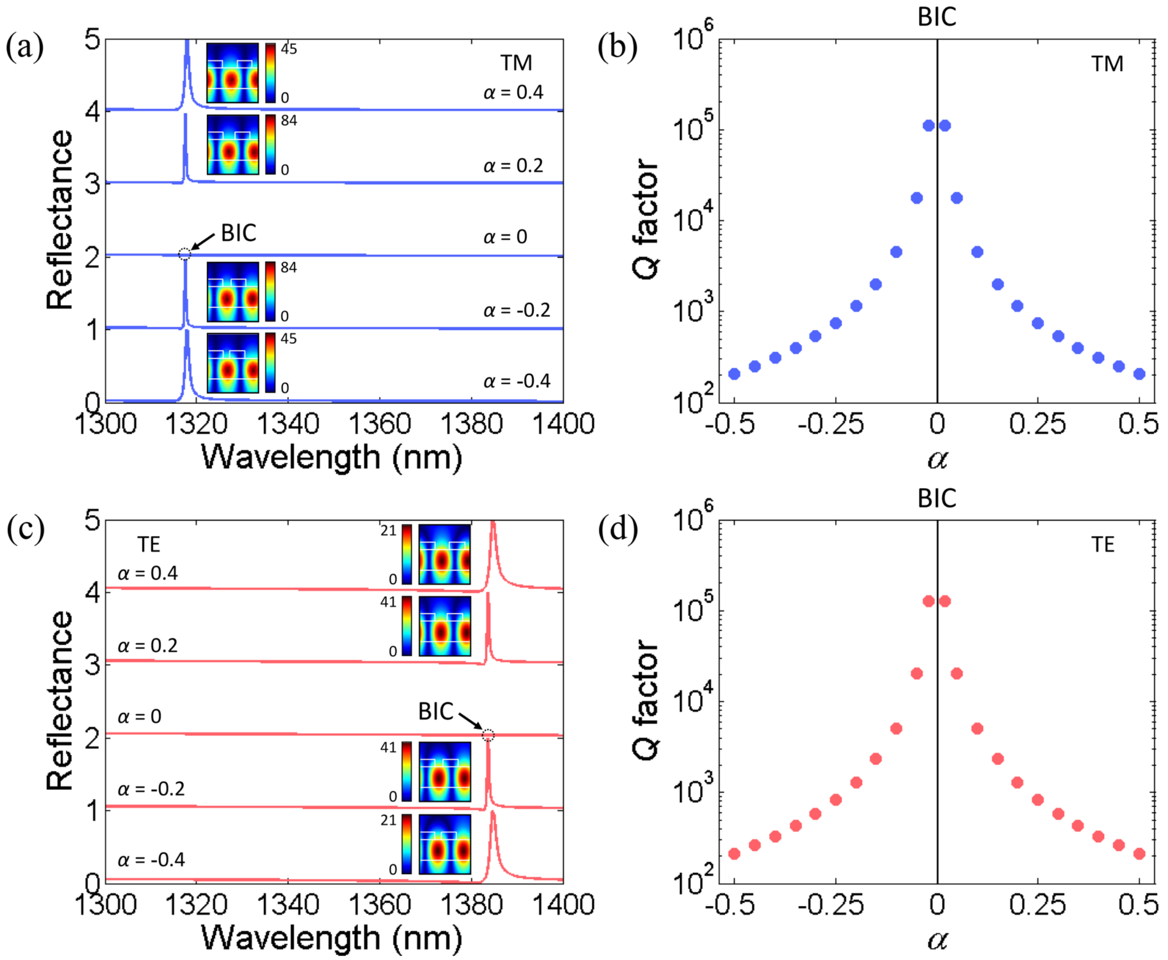

FIG. 2. Reflectance spectra of the compound grating waveguide structures with different perturbation parameters at normal incidence for (a) TM and (c) TE polarizations. The insets in (a) and (c) depict the magnetic and electric field distributions at the reflectance peaks under plane-wave incidences, respectively. Dependences of the Q factor of the quasi-BIC on the perturbation parameter for (b) TM and (d) TE polarizations.

analysis approach [102,103] to calculate the reflectance spectra of the compound grating waveguide structures with different perturbation parameters α at normal incidence for TM polarization, as shown in Fig. 2(a). The insets depict the magnetic field distributions at the reflectance peaks under plane-wave incidences. The magnetic field distributions are performed by the commercial COMSOL MULTIPHYSICS software. To quantify the field-enhancement effect, the strength of the incident magnetic field is normalized. Owing to the geometric symmetry of the structure, the reflectance spectrum with $\alpha = +\alpha_0$ is identical with that with $\alpha = -\alpha_0$. When $\alpha = \pm 0.4$, a Fano resonance appears at the wavelength of 1317.91 nm. Empowered by the GMR, the magnetic field is strongly enhanced and localized inside the waveguide layer. When $\alpha = \pm 0.2$, a narrower Fano resonance appears at the wavelength of 1317.53 nm, and the magnetic field is further enhanced. When $\alpha = 0$, no Fano resonance appears, which corresponds to the momentum mismatch driven BIC. The wavelength of the BIC can be extracted as 1317.40 nm, which agrees with that predicted by the theoretical model ($\lambda_{\pm 2}^{\mathrm{TM}} = 1322.4$ nm). The relative error is only 0.38%. Hence, the empty-lattice approximation is valid. In addition, we calculate the dependence of the Q factor of the quasi-BIC on the perturbation parameter, as shown in Fig. 2(b). The Q factor is calculated by $Q = f_{\mathrm{peak}}/\Delta f = f_{\mathrm{peak}}/|f_{\mathrm{peak}} - f_{\mathrm{dip}}|$, where f_{peak} and f_{dip} represent the frequencies of the reflectance peak and dip, respectively. When $\alpha = \pm 0.4$, the Q factor of the quasi-BIC is only 2.07×10^2. As α approaches to zero, the Q factor of the quasi-BIC increases significantly. When $\alpha = \pm 0.02$, the Q factor of the quasi-BIC reaches 1.11×10^5. When $\alpha = 0$, the Q factor becomes infinitely high, confirming the formation of a momentum mismatch driven BIC. Similarly, we calculate the reflectance spectra of the compound grating waveguide structures with different perturbation parameters α at normal incidence for TE polarization, as shown in Fig. 2(c). The insets depict the electric field distributions at the reflectance peaks under plane-wave incidences. The electric field distributions are performed by the commercial COMSOL MULTIPHYSICS software. To quantify the field-enhancement effect, the strength of the incident electric field is normalized. When $\alpha = \pm 0.4$, a Fano resonance appears at the wavelength of 1384.75 nm. Empowered by the GMR, the electric field is strongly enhanced and localized inside the waveguide layer. When $\alpha = \pm 0.2$, a narrower Fano resonance appears at the wavelength of 1383.65 nm, and the electric field is further enhanced. When $\alpha = 0$, no Fano resonance appears, which corresponds to the momentum mismatch driven BIC. The wavelength of the BIC can be extracted as 1383.29 nm, which agrees with that predicted by the theoretical model ($\lambda_{\pm 2}^{\mathrm{TE}} = 1394.0$ nm). The relative error is only 0.77%. In addition, we calculate the dependence of the Q factor of the quasi-BIC on the perturbation parameter, as shown in Fig. 2(d). When $\alpha = \pm 0.4$, the Q factor of the quasi-BIC is only 2.15×10^2. As α approaches to zero, the Q factor of the quasi-BIC increases significantly. When $\alpha = \pm 0.02$, the Q factor of the quasi-BIC reaches 1.27×10^5. When $\alpha = 0$, the Q factor becomes infinitely high, confirming the formation of a momentum mismatch driven BIC. To determine whether the momentum mismatch driven quasi-BICs and BIC are leaky or not, we simulate the eigenfrequencies and eigenmode profiles by the commercial COMSOL MULTIPHYSICS software (details can be seen in Sec. I of the Supplemental Material [104]). The momentum mismatch driven quasi-BICs are leaky while the momentum mismatch driven BIC is nonleaky.

According to Eqs. (2)-(5), the momentum-frequency relations for the TM$_0$ and TE$_0$ guided modes strongly depend on the height of the HfO$_2$ waveguide layer. Hence, the wavelengths of the momentum mismatch driven BICs at normal incidence for TM and TE polarizations strongly depend on the height of the HfO$_2$ waveguide layer (details can be seen in Sec. II A of the Supplemental Material [104]). As the height of the HfO$_2$ waveguide layer increases, the wavelengths of the momentum mismatch driven BICs at normal incidence for TM and TE polarizations increases.

B. Physical mechanism of dual momentum mismatch driven BICs in compound grating waveguide structure at oblique incidence

Now, we discuss the case of oblique incidence. Suppose that a linearly polarized plane wave obliquely launches onto the structure in the xOz plane at an incident angle $\theta = 5^\circ$. At oblique incidence, the momentum-matching condition for the unperturbed structure can be expressed as [98]

$$k_{x,m} = k_0 \sin\theta - m\frac{2\pi}{p} = \beta \quad (m = \pm 1, \pm 2, \ldots). \tag{7}$$

Distinct from the case of normal incidence, the momentum-frequency relations $k_{x,\pm 1}$ are not vertical lines due to the nonzero tangential momentum of the incident light, as shown by the black dashed lines in Fig. 3(a). For TM polarization, two momentum-matching points

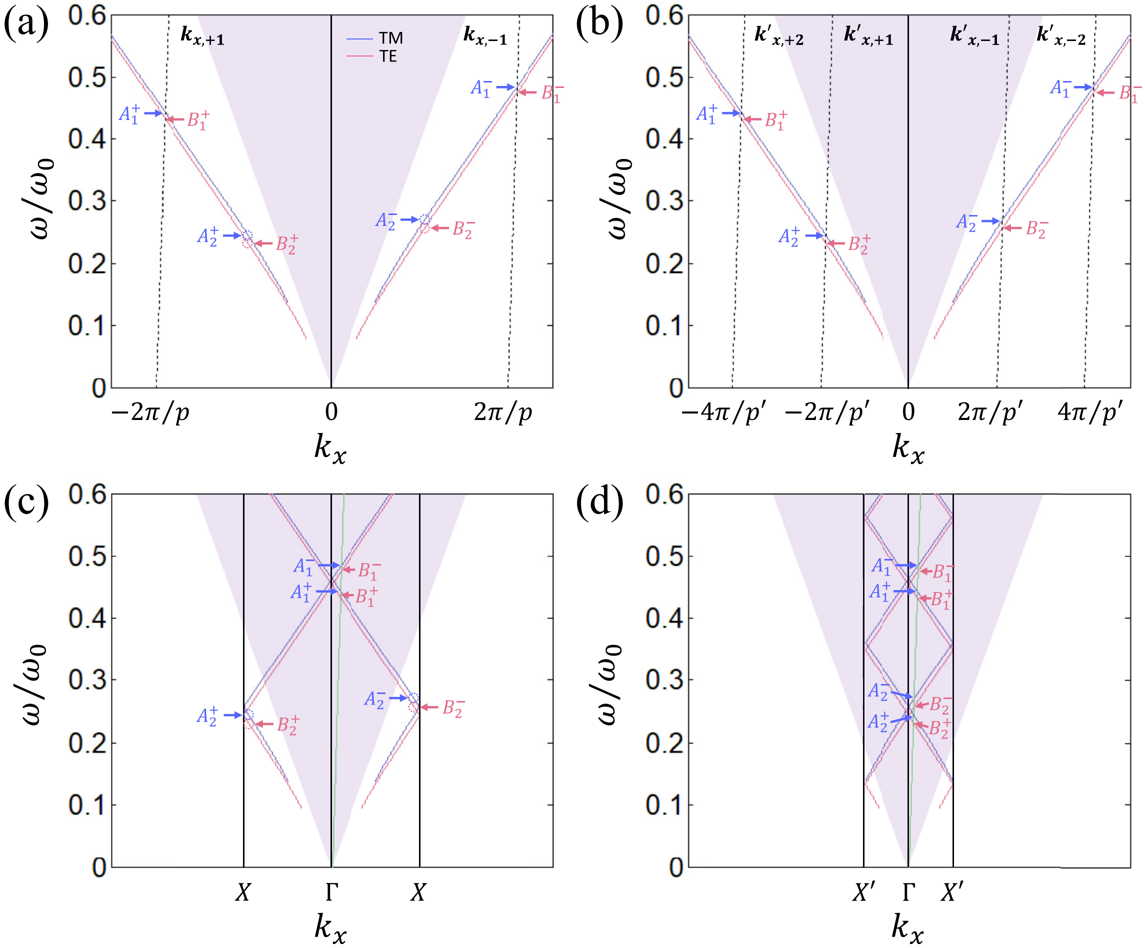

FIG. 3. Momentum-frequency relations in infinite momentum spaces for (a) unperturbed and (b) perturbed cases. The purple-shadowed region represents the light cone. Momentum-frequency relations folded into the first Brillouin zones for (c) unperturbed and (d) perturbed cases. The green solid line represents the momentum-frequency relation of the incident light $k_x = k_0 \sin\theta$. The incident angle is set to be $\theta = 5^\circ$.

(marked by $A_1^{\pm}$) occur at different angular frequencies $\omega_{+1}^{\mathrm{TM}} = 0.4434\omega_0$ ($\lambda_{+1}^{\mathrm{TM}} = 766.8$ nm) and $\omega_{-1}^{\mathrm{TM}} = 0.4848\omega_0$ ($\lambda_{-1}^{\mathrm{TM}} = 701.3$ nm), giving rise to two Fano resonances. For TE polarization, two momentum-matching points (marked by $B_1^{\pm}$) occur at different angular frequencies $\omega_{+1}^{\mathrm{TE}} = 0.4336\omega_0$ ($\lambda_{+1}^{\mathrm{TE}} = 781.4$ nm) and $\omega_{-1}^{\mathrm{TE}} = 0.4750\omega_0$ ($\lambda_{-1}^{\mathrm{TE}} = 715.8$ nm), also giving rise to two Fano resonances.

For the perturbed structure, the period of the grating layer doubles. Consequently, the momentum-matching condition becomes

$$\begin{aligned} k'_{x,m} &= k_0 \sin\theta - m' \frac{2\pi}{p'} \\ &= k_0 \sin\theta - m' \frac{\pi}{p} = \beta \quad (m' = \pm 1, \pm 2, \ldots). \end{aligned} \tag{8}$$

The basic momentum provided by the grating layer is reduced by half, i.e., $2\pi/p' = \pi/p$. Interestingly, the momentum-frequency relations $k'_{x,\pm 2m}$ overlap with the momentum-frequency relations $k_{x,\pm m}$. According to Eq. (8), we plot the momentum-frequency relations $k'_{x,\pm 1}$ and $k'_{x,\pm 2}$, as shown by the black dashed lines in Fig. 3(b). For TM polarization, four momentum-matching points (marked by $A_1^{\pm}$ and $A_2^{\pm}$) occur at four angular frequencies $\omega_{+1}^{\mathrm{TM}} = 0.4434\omega_0$ ($\lambda_{+1}^{\mathrm{TM}} = 766.8$ nm), $\omega_{-1}^{\mathrm{TM}} = 0.4848\omega_0$ ($\lambda_{-1}^{\mathrm{TM}} = 701.3$ nm), $\omega_{+2}^{\mathrm{TM}} = 0.2455\omega_0$ ($\lambda_{+2}^{\mathrm{TM}} = 1384.9$ nm), and $\omega_{-2}^{\mathrm{TM}} = 0.2698\omega_0$ ($\lambda_{-2}^{\mathrm{TM}} = 1260.2$ nm), giving rise to four Fano resonances. For TE polarization, four momentum-matching points (marked by $B_1^{\pm}$ and $B_2^{\pm}$) occur at four angular frequencies $\omega_{+1}^{\mathrm{TE}} = 0.4336\omega_0$ ($\lambda_{+1}^{\mathrm{TE}} = 784.1$ nm), $\omega_{-1}^{\mathrm{TE}} = 0.4750\omega_0$ ($\lambda_{-1}^{\mathrm{TE}} = 715.8$ nm), $\omega_{+2}^{\mathrm{TE}} = 0.2330\omega_0$ ($\lambda_{+2}^{\mathrm{TE}} = 1459.2$ nm), and $\omega_{-2}^{\mathrm{TE}} = 0.2558\omega_0$ ($\lambda_{-2}^{\mathrm{TE}} = 1329.2$ nm), also giving rise to four Fano resonances.

Considering a parameter changing process $\alpha \neq 0 \rightarrow \alpha = 0$, the perturbed structure turns into an unperturbed structure. Consequently, the previously excitable guided resonances at angular frequencies $\omega_{+2}^{\mathrm{TM}} = 0.2445\omega_0$ ($\lambda_{+2}^{\mathrm{TM}} = 1384.9$ nm), $\omega_{-2}^{\mathrm{TM}} = 0.2698\omega_0$ ($\lambda_{-2}^{\mathrm{TM}} = 1260.2$ nm), $\omega_{+2}^{\mathrm{TE}} = 0.2330\omega_0$ ($\lambda_{+2}^{\mathrm{TE}} = 1459.2$ nm), and $\omega_{-2}^{\mathrm{TE}} = 0.2558\omega_0$ ($\lambda_{-2}^{\mathrm{TE}} = 1329.2$ nm) become momentum mismatch driven BICs since the momentum-matching conditions are broken.

Next, we demonstrate the equivalence of momentum mismatch driven BICs and BICs induced by band folding [48–54]. Similar to Sec. II A, we fold the momentum-frequency relations of TM$_0$ and TE$_0$ guided modes into the first Brillouin zone for the unperturbed and perturbed cases, as shown in Figs. 3(c) and 3(d), respectively. For the unperturbed structure, the edges of the first Brillouin zone are located at $k_x = \pm\pi/p$. Now, we consider the oblique incidence. Hence, we plot the momentum-frequency relation of the incident light at oblique incidence, i.e., $k_x = k_0 \sin\theta$, as shown by the green solid line. Only the modes located at the crossing points between the momentum-frequency relations of the guided modes and that of the incident light are excitable. Comparing Fig. 3(c) with 3(a), we can conclude that these excitable modes in Fig. 3(c) are identical with modes $A_1^{\pm}$ and $B_1^{\pm}$ in Fig. 3(a). Owing to the periodicity, modes $A_1^{\pm}$ and $B_1^{\pm}$ are folded inside the light cone. In addition, dark modes $A_2^{\pm}$ and $B_2^{\pm}$ cannot be excited by the incident light since they lie below the light cone. For the perturbed structure, the edges of the first Brillouin zone are located at $k_x = \pm\pi/p' = \pm\pi/2p$. Hence, the first Brillouin zone is reduced by half. Comparing Fig. 3(d) with 3(b), we can conclude that the excitable modes in Fig. 3(d) are identical with modes $A_1^{\pm}$, $B_1^{\pm}$, $A_2^{\pm}$, and $B_2^{\pm}$ in Fig. 3(b). Owing to the periodicity, modes $A_1^{\pm}$, $B_1^{\pm}$, $A_2^{\pm}$, and $B_2^{\pm}$ are folded inside the light cone. Considering the parameter changing process $\alpha = 0 \rightarrow \alpha \neq 0$, the momentum mismatch driven BICs turn into momentum mismatch driven quasi-BICs that lie inside the light cone.

Combining Figs. 1 and 3, we observe an interesting phenomenon: as the incidence changes from normal to oblique, the single momentum mismatch driven BIC splits into dual momentum mismatch driven BICs due to the nonzero tangential momentum of the incident light.

To further confirm the formation of the dual momentum mismatch driven BICs, we calculate the reflectance spectra of the compound grating waveguide structures with different perturbation parameters α at oblique incidence for TM polarization, as shown in Fig. 4(a). The insets depict the magnetic field distributions at the reflectance peaks under plane-wave incidences. When $\alpha = \pm 0.6$, two Fano resonances appear at the wavelengths of 1256.11 and 1380.67 nm. Empowered by the GMR, the magnetic field is strongly enhanced and localized inside the waveguide layer. When $\alpha = \pm 0.3$, two narrower Fano resonances appear at the wavelengths of 1256.27 and 1380.72 nm, and the magnetic field is further enhanced. When $\alpha = 0$, no Fano resonance appears, which corresponds to the dual momentum mismatch driven BICs. The wavelengths of the dual BICs can be extracted as 1256.38 and 1380.78 nm, which agrees with those predicted by the theoretical model ($\lambda_{-2}^{\mathrm{TM}} = 1260.2$ nm and $\lambda_{+2}^{\mathrm{TM}} = 1384.9$ nm). The relative errors are both 0.30%. In addition, we calculate the dependence of the Q factors of the dual quasi-BICs on the perturbation parameter, as shown in Fig. 4(b). When $\alpha = \pm 0.6$, the Q factors of quasi-BICs 1 and 2 are only 2.97×10^2 and 2.41×10^2, respectively. As α approaches zero, the Q factors of the dual quasi-BICs increase significantly. When $\alpha = \pm 0.02$, the Q factors of quasi-BICs 1 and 2 reach 1.43×10^5 and 1.71×10^5, respectively. When $\alpha = 0$, the Q factors become infinitely high, confirming the formation of dual momentum mismatch driven BICs. Similarly, we calculate the reflectance spectra of the compound grating waveguide structures with different perturbation parameters α at oblique incidence for TE polarization, as shown in Fig. 4(c). The insets depict the electric field distributions at the reflectance peaks under plane-wave incidences. When $\alpha = \pm 0.6$, two Fano resonances appear at the wavelengths of 1334.02 and 1466.18 nm. Empowered by the GMR, the electric field is strongly enhanced and localized inside the waveguide layer. When $\alpha = \pm 0.3$, two narrower Fano resonances appear at the wavelengths of 1334.40 and 1467.45 nm, and the electric field is further enhanced. When $\alpha = 0$, no Fano resonance appears, which corresponds to dual momentum mismatch driven BICs. The wavelengths of the dual BICs can be extracted as 1334.54 and 1467.95 nm, which agrees with those predicted by the theoretical model ($\lambda_{-2}^{\mathrm{TE}} = 1329.4$ nm and $\lambda_{+2}^{\mathrm{TE}} = 1459.2$ nm). The relative errors are only 0.39% and 0.60%, respectively. In addition, we calculate the dependence of the Q factors of the dual quasi-BICs on the perturbation parameter, as shown

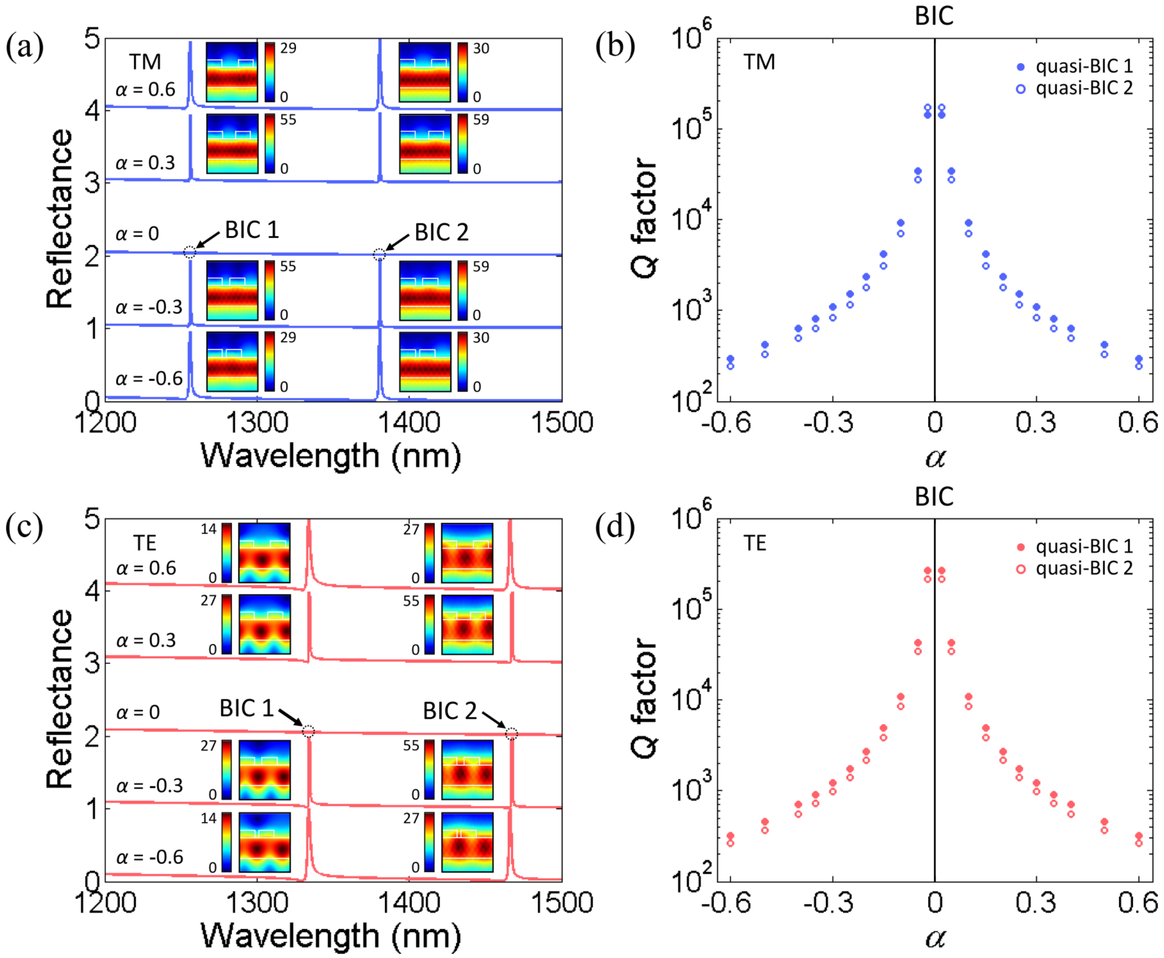

FIG. 4. Reflectance spectra of the compound grating waveguide structures with different perturbation parameters at oblique incidence ($\theta = 5^\circ$) for (a) TM and (c) TE polarizations. The insets in (a) and (c) depict the magnetic and electric field distributions at the reflectance peaks under plane-wave incidences, respectively. Dependences of the Q factors of the dual quasi-BICs on the perturbation parameter for (b) TM and (d) TE polarizations.

in Fig. 4(d). When $\alpha = \pm 0.6$, the Q factors of quasi-BICs 1 and 2 are only 3.22×10^2 and 2.61×10^2, respectively. As α approaches zero, the Q factors of the dual quasi-BICs increase significantly. When $\alpha = \pm 0.02$, the Q factors of quasi-BICs 1 and 2 reach 2.69×10^5 and 2.12×10^5, respectively. When $\alpha = 0$, the Q factors become infinitely high, confirming the formation of the dual momentum mismatch driven BICs.

According to Eqs. (2)-(5), the momentum-frequency relations for the TM_0 and TE_0 guided modes strongly depend on the height of the HfO_2 waveguide layer. Hence, the wavelengths of the dual momentum mismatch driven BICs at oblique incidence for TM and TE polarizations strongly depend on the height of the HfO_2 waveguide layer (details can be seen in Sec. II B of the Supplemental Material [104]). As the height of the HfO_2 waveguide layer increases, the wavelengths of the dual momentum mismatch driven BICs at normal incidence for TM and TE polarizations increase.

C. Robustness of Q factor of momentum mismatch driven quasi-BIC against incident angle

It is known that conventional symmetry-protected [4,40] and accidental BICs [41,42] are located at specific isolated points in photonic bands. In other words, the transition from symmetry-protected and accidental BICs to symmetry-protected and accidental quasi-BICs depends on an in-plane wave vector. Hence, conventional symmetry-protected and accidental quasi-BICs can only maintain ultrahigh Q factors in ultranarrow angle ranges. However, the transition from momentum mismatch driven BICs to momentum mismatch driven quasi-BICs does not depend on an in-plane wave vector. Such transition is induced by discontinuous variation of photonic bands originating from the first Brillouin zone folding, as shown in Figs. 1 and 3. Consequently, Q factors of momentum mismatch driven quasi-BICs exhibit angular robustness far beyond conventional symmetry-protected and accidental quasi-BICs.

As we discussed in Sec. II B, for the perturbed structure with $\alpha \neq 0$, the single momentum mismatch driven quasi-BIC splits into dual momentum mismatch driven quasi-BICs as the incidence changes from normal to oblique. Figures 5(a) and 5(b) give the dependences of the Q factors of quasi-BICs 1 and 2 on the incident angle for TM and TE polarizations, respectively. The perturbation parameter is set to be $\alpha = 0.2$. For TM polarization, as the incident angle increases from 0.5° to 6°, the Q factor of quasi-BIC 1 slightly increases from 2.06×10^3 to 2.38×10^3 and then slightly decreases to

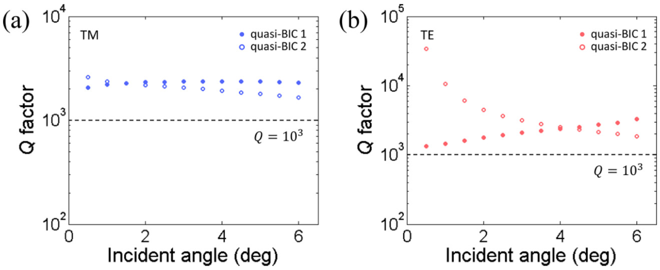

FIG. 5. Dependences of the Q factors of quasi-BICs 1 and 2 on the incident angle for (a) TM and (b) TE polarizations.

2.30×10^3. The Q factor of quasi-BIC 2 slightly decreases from 2.59×10^3 to 1.65×10^3. For TE polarization, as the incident angle increases from 0.5° to 6°, the Q factor of the quasi-BIC 1 slightly increases from 1.34×10^3 to 3.32×10^3 while the Q factor of quasi-BIC 2 gradually decreases from 3.38×10^4 to 1.87×10^3. When the incident angle ranges from 0.5° to 6°, the Q factors of all the quasi-BICs are higher than 10^3, indicating that the Q factors of the momentum mismatch driven quasi-BICs demonstrate robustness against the incident angle.

III. PAIR OF ELLIPSOMETRIC PHASE SINGULARITIES EMPOWERED BY MOMENTUM MISMATCH DRIVEN BIC

In this section, we exploit the momentum mismatch driven BIC to realize a pair of ellipsometric phase singularities. Two ellipsometric parameters, i.e., ellipsometric amplitude Ψ and ellipsometric phase Δ, take the following form [89]:

$$\frac{r^{\mathrm{TM}}}{r^{\mathrm{TE}}} = e^{i\Delta}\tan\Psi, \tag{9}$$

where r^{TM} (r^{TE}) denotes the reflection coefficient for TM (TE) polarization. The reflection coefficients for TM and TE polarizations can be expanded as

$$r^{\mathrm{TM}} = |r^{\mathrm{TM}}|e^{i\varphi^{\mathrm{TM}}}, \tag{10}$$

$$r^{\mathrm{TE}} = |r^{\mathrm{TE}}|e^{i\varphi^{\mathrm{TE}}}, \tag{11}$$

where φ^{TM} (φ^{TE}) denotes the reflection phase for TM (TE) polarization. By substituting Eqs. (10) and (11) into Eq. (9), ellipsometric amplitude Ψ and ellipsometric phase Δ can be calculated by

$$\Psi = \arctan\frac{|r^{\mathrm{TM}}|}{|r^{\mathrm{TE}}|}, \tag{12}$$

$$\Delta = \varphi^{\mathrm{TM}} - \varphi^{\mathrm{TE}}. \tag{13}$$

Figures 6(a) and 6(b) give the dependences of the reflectance spectrum and reflection phase spectrum of the compound grating waveguide structure on the perturbation parameter α at normal incidence for TM polarization. For $\alpha \neq 0$, a momentum mismatch driven quasi-BIC occurs. In the vicinity of the wavelength of the momentum mismatch driven quasi-BIC, the reflection phase changes significantly with the wavelength. Away from the wavelength of the momentum mismatch driven quasi-BIC, the reflection phase changes smoothly with the wavelength. For $\alpha = 0$, a momentum mismatch driven BIC occurs at the wavelength of 1317.40 nm. As a result, the reflection phase always changes smoothly with the wavelength. Figures 6(c) and 6(d) give the dependences of the reflectance spectrum and reflection phase spectrum of the compound grating waveguide structure on the perturbation parameter α at normal incidence for TE polarization. For $\alpha \neq 0$, a momentum mismatch driven quasi-BIC occurs. In the vicinity of the wavelength of the momentum mismatch driven quasi-BIC, the reflection phase changes significantly with the wavelength. Away from the wavelength of the momentum mismatch driven quasi-BIC, the reflection phase changes smoothly with the wavelength. For $\alpha = 0$, a momentum mismatch driven BIC occurs at the wavelength of 1383.29 nm. As a result, the reflection phase always changes smoothly with the wavelength. According to Eqs. (12) and (13), we calculate the dependences of the ellipsometric amplitude spectrum and ellipsometric phase spectrum of the compound grating waveguide structure on the perturbation parameter α at normal incidence, as depicted in Figs. 6(e) and 6(f), respectively. For $\alpha \neq 0$, in the vicinity of the wavelengths of TM and TE momentum mismatch driven quasi-BICs, both the ellipsometric amplitude and phase change significantly with the wavelength. Away from the wavelengths of the TM and TE momentum mismatch driven quasi-BICs, both the ellipsometric amplitude and the phase change smoothly with the wavelength. For $\alpha = 0$, both the ellipsometric amplitude and the phase always change smoothly with the wavelength. Empowered by the momentum mismatch driven BIC, a pair of ellipsometric amplitude (phase) singularities emerge.

Considering the difficulty in fabrication, we choose the perturbation parameter as $\alpha = 0.3$. The widths of two air grooves are $w_{\mathrm{L}1} = f_{\mathrm{L}1}p = 0.52p$ and $w_{\mathrm{L}2} = f_{\mathrm{L}2}p = 0.28p$, respectively. The width difference between two air grooves reaches $\Delta w = w_{\mathrm{L}1} - w_{\mathrm{L}2} = 0.24p = 102.6$ nm, which is well within the reach of the current fabrication technique [105]. Figure 7(a) shows the reflectance spectra of the compound grating waveguide structure at normal incidence for TM and TE polarizations. The TM and TE momentum mismatch driven quasi-BICs appear at the wavelengths of 1317.69 and 1384.11 nm, respectively. Figure 7(b) depicts the reflection phase spectra of the compound grating waveguide structure at normal incidence for TM and TE polarizations. The reflection phase changes significantly with the wavelength around the wavelength of the momentum mismatch driven quasi-BIC. Figures 7(c) and 7(d) show the ellipsometric amplitude and phase spectra of the compound grating waveguide structure at normal incidence, respectively. Both the ellipsometric amplitude and the phase change significantly with the wavelength around the wavelengths of the TM and TE momentum mismatch driven quasi-BICs.

IV. ULTRASENSITIVE REFRACTIVE INDEX SENSING ENABLED BY DRASTIC ELLIPSOMETRIC PHASE CHANGE

As an example of the applications of the ellipsometric phase singularity, we achieve ultrasensitive refractive index sensing. The compound grating waveguide structure is integrated with microfluidics [106], as schematically shown

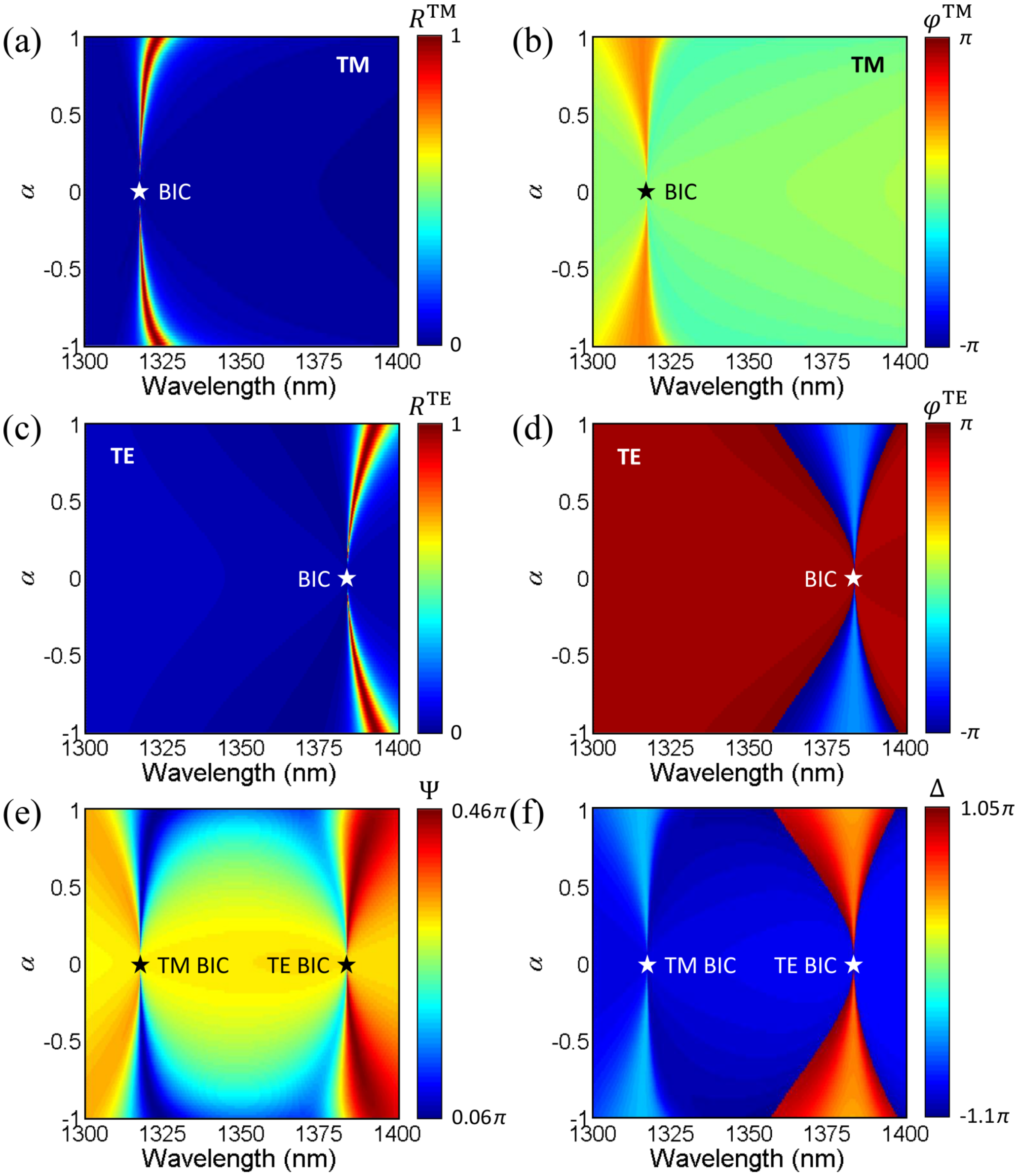

FIG. 6. Dependences of (a) reflectance spectrum and (b) reflection phase spectrum of the compound grating waveguide structure on the perturbation parameter α at normal incidence for TM polarization. Dependences of (c) reflectance spectrum and (d) reflection phase spectrum of the compound grating waveguide structure on the perturbation parameter α at normal incidence for TE polarization. Dependences of (e) ellipsometric amplitude spectrum and (f) ellipsometric phase spectrum of the compound grating waveguide structure on the perturbation parameter α at normal incidence.

in Fig. 8(a). Specifically, the compound grating waveguide structure is placed into a gas chamber. Therefore, the medium above the compound grating waveguide structure is the sensing gas with a refractive index n_{gas} while that below the compound grating waveguide structure is SiO_2 with a refractive index $n_S = 1.44$. The refractive index of the sensing gas is related to the gas material and its concentration. According to the experimental measurements [107], the refractive index of hydrogen (H_2) gas can be changed from 1 to 1.08 as its concentration increases from 0 to 0.05 $\mathrm{g/cm^3}$. The perturbation parameter is set to be $\alpha = 0.3$. Then, we calculate the ellipsometric phase spectra of the designed refractive index sensor with different refractive indices of the sensing gas at normal incidence, as given in Fig. 8(b). As the refractive index of the sensing gas slightly changes from 1 to 1.004, the peak of ellipsometric phase shifts from 1317.13 to 1317.62 nm. We select an operating wavelength of 1317.8 nm and calculate the dependence of the ellipsometric phase on the refractive index of the sensing gas at the operating wavelength, as given in Fig. 8(c). As the refractive index of the sensing gas slightly changes from 1 to 1.004, the ellipsometric phase at the operating wavelength strongly increases from 1.161π to 1.537π. As demonstrated, the dependence of the ellipsometric phase on the refractive index of the sensing gas is nonlinear. It is known that linear response is more convenient in sensing experiments. Hence, we define the linear region as the operating refractive index range, i.e., from 1 to 1.003, which is marked by the purple dashed box.

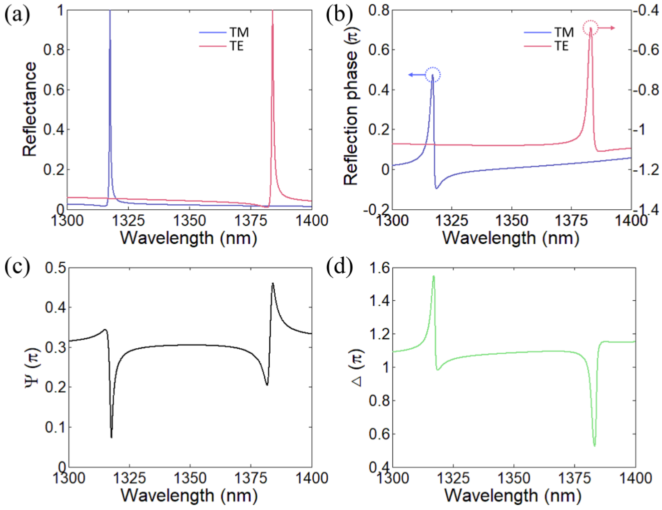

FIG. 7. (a) Reflectance spectra of the compound grating waveguide structure at normal incidence for TM and TE polarizations. (b) Reflection phase spectra of the compound grating waveguide structure at normal incidence for TM and TE polarizations. (c) Ellipsometric amplitude and (b) phase spectra of the compound grating waveguide structure at normal incidence. The perturbation parameter is set to be $\alpha = 0.3$.

Next, we calculate the sensitivity and resolution of the designed refractive index sensor at the operating wavelength of 1317.8 nm in the operating refractive index range. The sensitivity of the designed refractive index sensor can be calculated by [108]

$$S = \left|\frac{d\Delta}{dn_{\text{gas}}}\right|. \tag{14}$$

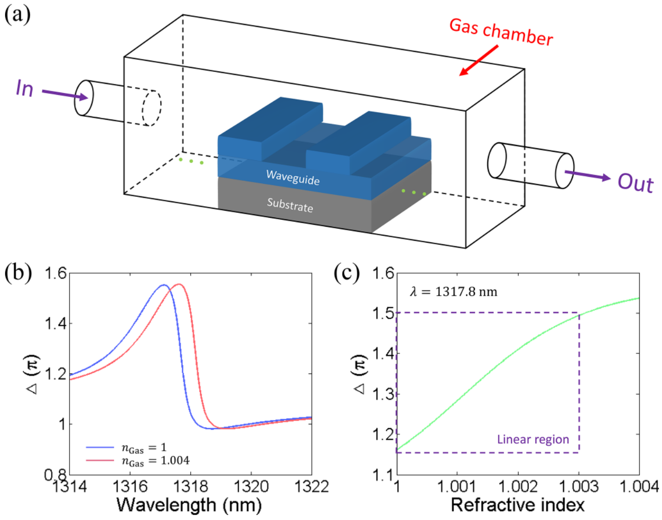

FIG. 8. (a) Schematic of the designed refractive index sensor. (b) Ellipsometric phase spectra of the designed refractive index sensor with different refractive indices of the sensing gas at normal incidence. (c) Dependence of the ellipsometric phase on the refractive index of the sensing gas at the operating wavelength of 1317.8 nm. Purple dashed box represents the linear region. The perturbation parameter is set to be $\alpha = 0.3$.

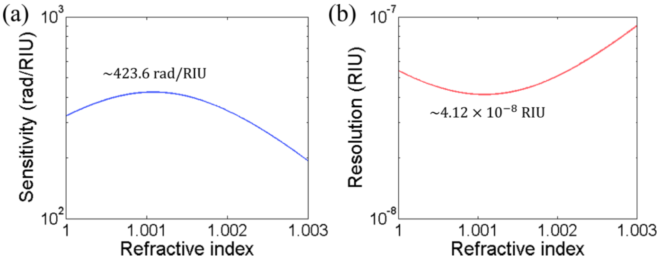

FIG. 9. (a) Dependence of the sensitivity of the designed refractive index sensor (in units of rad/RIU) on the refractive index of the sensing gas. (b) Dependence of the resolution of the designed refractive index sensor (in units of RIU) on the refractive index of the sensing gas. The perturbation parameter is set to be $\alpha = 0.3$. The operating wavelength is set to be 1317.8 nm.

According to Eq. (14), we calculate the dependence of the sensitivity of the designed refractive index sensor (in units of rad/RIU) on the refractive index of the sensing gas, as given in Fig. 9(a). As the refractive index of the sensing gas increases from 1 to 1.003, the sensitivity increases from 323.6 to 423.6 rad/RIU, and then decreases to 192.7 rad/RIU. The maximum sensitivity reaches 423.6 rad/RIU.

Under the current measure technique, the limit of the resolution of the ellipsometric phase is $\delta\Delta = 0.001^\circ = 1.75 \times 10^{-5}$ rad [109]. Hence, the resolution of the refractive index sensor can be determined by [110]

$$\delta n_{\text{gas}} = \frac{\delta\Delta}{S}. \tag{15}$$

According to Eq. (15), we calculate the dependence of the resolution of the designed refractive index sensor (in units of RIU) on the refractive index of the sensing gas, as given in Fig. 9(b). As the refractive index of the sensing gas increases from 1 to 1.003, the resolution decreases from 5.39×10^{-8} to 4.12×10^{-8} RIU, and then increases to 9.06×10^{-8} RIU. The minimum resolution reaches 4.12×10^{-8} RIU. Enabled by a drastic ellipsometric phase change, we achieve ultrasensitive refractive index sensing.

As we discussed in Sec. II A, the wavelengths of the momentum mismatch driven quasi-BICs at normal incidence for TM and TE polarizations strongly depend on the height of the HfO_2 waveguide layer. As a result, the ultrasensitive refractive index sensing enabled by a drastic ellipsometric phase change depends on the height of the HfO_2 waveguide layer (details can be seen in Sec. II C of the Supplemental Material [104]). The results show that the operating wavelength of the ultrasensitive refractive index sensing strongly depends on the height of the HfO_2 waveguide layer while the minimum resolution is robust against the height of the HfO_2 waveguide layer.

As seen from Fig. 8(c), the linear region of the dependence of the ellipsometric phase on the refractive index of the sensing gas is narrow. It should be noted that the width of the operating refractive index range and sensitivity satisfy a negative correlation. Hence, if one would like to expand the operating refractive index range, the sensitivity should be reduced. To reduce the sensitivity, a large perturbation parameter should be chosen. Now, the perturbation parameter

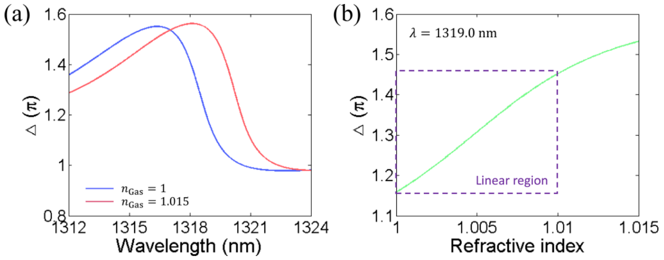

FIG. 10. (a) Ellipsometric phase spectra of the designed refractive index sensor with different refractive indices of the sensing gas at normal incidence. (b) Dependence of the ellipsometric phase on the refractive index of the sensing gas at the operating wavelength of 1319.0 nm. Purple dashed box represents the linear region. The perturbation parameter is set to be $\alpha = 0.6$.

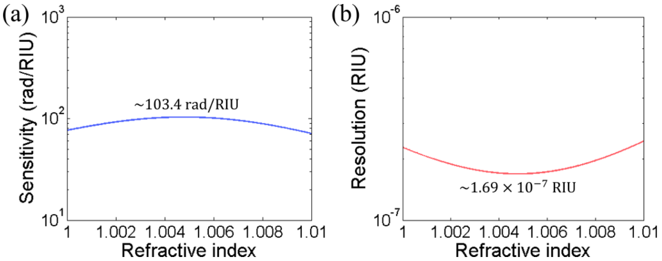

FIG. 11. (a) Dependence of the sensitivity of the designed refractive index sensor (in units of rad/RIU) on the refractive index of the sensing gas. (b) Dependence of the resolution of the designed refractive index sensor (in units of RIU) on the refractive index of the sensing gas. The perturbation parameter is set to be $\alpha = 0.6$. The operating wavelength is set to be 1319.0 nm.

is changed to be $\alpha = 0.6$ to achieve a broader operating refractive index range. Figure 10(a) gives the ellipsometric phase spectra of the designed refractive index sensor with different refractive indices of the sensing gas at normal incidence. As the refractive index of the sensing gas slightly changes from 1 to 1.015, the peak of the ellipsometric phase shifts from 1316.38 to 1318.12 nm. We select an operating wavelength of 1319.0 nm and calculate the dependence of the ellipsometric phase on the refractive index of the sensing gas at the operating wavelength, as given in Fig. 10(b). As the refractive index of the sensing gas slightly changes from 1 to 1.015, the ellipsometric phase at the operating wavelength strongly increases from 1.158π to 1.532π. Comparing Fig. 10(b) with 8(c), the linear region is effectively expanded. The operating refractive index range is from 1 to 1.01.

Next, we calculate the sensitivity and resolution of the designed refractive index sensor at the operating wavelength of 1319.0 nm in the operating refractive index range. Figure 11(a) gives the dependence of the sensitivity of the designed refractive index sensor (in units of rad/RIU) on the refractive index of the sensing gas. As the refractive index of the sensing gas increases from 1 to 1.01, the sensitivity increases from 76.5 to 103.4 rad/RIU, and then decreases to 71.4 rad/RIU. The maximum sensitivity reaches 103.4 rad/RIU. Figure 11(b) gives the dependence of the resolution of the designed refractive index sensor (in units of RIU) on the refractive index of the sensing gas. As the refractive index of the sensing gas increases from 1 to 1.01, the resolution decreases from 2.28×10^{-7} to 1.69×10^{-7} RIU, and then increases to 2.45×10^{-7} RIU. The minimum resolution reaches 1.69×10^{-7} RIU. Comparing Fig. 11(b) with 9(b), the maximum sensitivity is reduced.

As we discussed in Sec. II, there are two key points to realize momentum mismatch driven quasi-BICs. One is that a lossless dielectric waveguide layer supports the guided modes. The other is that the lossless dielectric ridges with complex lattices provide the basic momentum. Therefore, ultrasensitive refractive index sensing enabled by a drastic ellipsometric phase change can also be achieved at visible wavelengths (details can be seen in Sec. III of the Supplemental Material [104]).

V. CONCLUSIONS

In summary, we demonstrate the physical mechanism of momentum mismatch driven BICs in compound grating waveguide structures. As the incidence changes from normal to oblique, the single momentum mismatch driven BIC splits into dual momentum mismatch driven BICs. Unlike conventional symmetry-protected and accidental quasi-BICs, the Q factors of momentum mismatch driven quasi-BICs exhibit robustness against the incident angle. Empowered by the momentum mismatch driven BIC, we realize a pair of ellipsometric phase singularities. As an example of the applications, we exploit the drastic ellipsometric phase change to achieve ultrasensitive refractive index sensing. The minimum resolution of the designed refractive index sensor reaches the order of 10^{-8} RIU. These results not only provide unique insights into the relation between momentum, BICs, and ellipsometric phase, but also indicate a methodology to design high-performance phase-based optical devices.

ACKNOWLEDGMENTS

This work is supported by the National Natural Science Foundation of China (Grants No. 12104105, No. 12364045, No. 12304420, No. 12264028, No. 12364049, No. 12274325, No. 91850206, and No. 11974261), the National Key Research and Development Program of China (Grant No. 2021YFA1400602), the Guangdong Basic and Applied Basic Research Foundation (Grant No. 2023A1515011024), the Science and Technology Program of Guangzhou (Grant No. 202201011176), the Natural Science Foundation of Jiangxi Province (Grants No. 20232BAB211025 and No. 20232BAB201040), the Start-up Funding of Guangdong Polytechnic Normal University (Grant No. 2021SDKYA033), and the Start-up Funding of Nanchang Institute of Science and Technology (Grant No. NGRCZX-23–01).

---

[1] C. W. Hsu, B. Zhen, A. D. Stone, J. D. Joannopoulos, and M. Soljačić, Bound states in the continuum, Nat. Rev. Mater. **1**, 16048 (2016).

[2] A. F. Sadreev, Interference traps waves in an open system: Bound states in the continuum, Rep. Prog. Phys. **84**, 055901 (2021).

[3] S. Joseph, S. Pandey, S. Sarkar, and J. Joseph, Bound states in the continuum in resonant nanostructures: An overview of engineered materials for tailored applications, Nanophotonics **10**, 4175 (2021).

[4] K. Koshelev, S. Lepeshov, M. Liu, A. Bogdanov, and Y. Kivshar, Asymmetric metasurfaces with high-Q resonances governed by bound states in the continuum, Phys. Rev. Lett. **121**, 193903 (2018).

[5] N. Levanon, S. R. K. C. Indukuri, C. Frydendahl, J. Bar-David, Z. Han, N. Mazurski, and U. Levy, Angular transmission response of in-plane symmetry-breaking quasi-BIC all-dielectric metasurfaces, ACS Photonics **9**, 3642 (2022).

[6] L. Huang, W. Zhang, and X. Zhang, Moiré quasibound states in the continuum, Phys. Rev. Lett. **128**, 253901 (2022).

[7] P. Hu, J. Wang, Q. Jiang, J. Wang, L. Shi, D. Han, Z. Q. Zhang, C. T. Chan, and J. Zi, Global phase diagram of bound states in the continuum, Optica **9**, 1353 (2022).

[8] A. Kodigala, T. Lepetit, Q. Gu, B. Bahari, Y. Fainman, and B. Kanté, Lasing action from photonic bound states in continuum, Nature (London) **541**, 196 (2017).

[9] J.-H. Yang, Z.-T. Huang, D. N. Naksimov, P. S. Pankin, I. V. Timofeev, K.-B. Hong, H. Li, J.-W. Chen, C.-Y. Hsu, Y.-Y. Liu, T.-C. Lu, T.-R. Lin, C.-S. Yang, and K.-P. Chen, Low-threshold bound state in the continuum lasers in hybrid lattice resonance metasurfaces, Laser Photonics Rev. **15**, 2100118 (2021).

[10] Y. Ren, P. Li, Z. Liu, Z. Chen, Y.-L. Chen, C. Peng, and J. Liu, Low-threshold nanolasers based on miniaturized bound states in the continuum, Sci. Adv. **8**, eade8817 (2022).

[11] H. Zhong, Y. Yu, Z. Zheng, Z. Ding, X. Zhao, J. Yang, Y. Wei, Y. Chen, and S. Yu, Ultra-low threshold continuous-wave quantum dot mini-BIC lasers, Light Sci. Appl. **12**, 100 (2023).

[12] S. Romano, G. Zito, S. Torino, G. Calafiore, E. Penzo, G. Coppola, S. Cabrini, I. Rendina, and V. Mocella, Label-free sensing of ultralow-weight molecules with all-dielectric metasurfaces supporting bound states in the continuum, Photonics Res. **6**, 726 (2018).

[13] L. Cong and R. Singh, Symmetry-protected dual bound states in the continuum in metamaterials, Adv. Opt. Mater. **7**, 1900383 (2019).

[14] D. N. Maksimov, V. S. Gerasimov, S. Romano, and S. P. Polyutov, Refractive index sensing with optical bound states in the continuum, Opt. Express **28**, 38907 (2020).

[15] I. Yusepov, D. Filonov, A. Bogdanov, P. Ginzburg, M. V. Rybin, and A. Slobozhanyuk, Chipless wireless temperature sensor based on quasi-BIC resonance, Appl. Phys. Lett. **119**, 193504 (2021).

[16] T. C. Tan, Y. K. Srivastava, R. T. Ako, W. Wang, M. Bhaskaran, S. Sriram, I. Al-Naib, E. Plum, and R. Singh, Active control of nanodielectric-induced THz quasi-BIC in flexible metasurfaces: A platform for modulation and sensing, Adv. Mater. **33**, 2100836 (2021).

[17] K. Wang, H. Liu, Z. Li, M. Liu, Y. Zhang, and H. Zhang, All-dielectric metasurface-based multimode sensing with symmetry-protected and accidental bound states in the continuum, Results Phys. **46**, 106276 (2023).

[18] S. Chen, Z. Li, Y. Mao, X. Dai, and Y. Xiang, Giant enhancement of the Goos-Hänchen shift assisted by merging bound states in the continuum, J. Appl. Phys. **133**, 193101 (2023).

[19] J. Li, Z. Yue, J. Li, C. Zheng, Y. Zhang, and J. Yao, Ultranarrowband terahertz circular dichroism driven by planar metasurface supporting chiral quasi bound states in the continuum, Opt. Laser Technol. **161**, 109173 (2023).

[20] M. V. Gorkunov, A. A. Antonov, and Y. S. Kivshar, Metasurfaces with maximum chirality empowered by bound states in the continuum, Phys. Rev. Lett. **125**, 093903 (2020).

[21] A. Overvig, N. Yu, and A. Alù, Chiral quasi-bound states in the continuum, Phys. Rev. Lett. **126**, 073001 (2021).

[22] J. Dixon, M. Lawrence, D. R. Barton, III and J. Dionne, Self-isolated Raman lasing with a chiral dielectric metasurface, Phys. Rev. Lett. **126**, 123201 (2021).

[23] J. Wu, X. Xu, X. Su, S. Zhao, C. Wu, Y. Sun, Y. Li, F. Wu, Z. Guo, H. Jiang, and H. Chen, Observation of giant extrinsic chirality empowered by quasi-bound states in the continuum, Phys. Rev. Appl. **16**, 064018 (2021).

[24] X. Zhang, Y. Liu, J. Han, Y. Kivshar, and Q. Song, Chiral emission from resonant metasurfaces, Science **377**, 1215 (2022).

[25] T. Shi, Z.-L. Deng, G. Geng, X. Zeng, Y. Zeng, G. Hu, A. Overvig, J. Li, C.-W. Qiu, A. Alù, Y. S. Kivshar, and X. Li, Planar chiral metasurfaces with maximal and tunable chiroptical response driven by bound states in the continuum, Nat. Commun. **13**, 4111 (2022).

[26] Y. Chen, H. Deng, X. Sha, W. Chen, R. Wang, Y.-H. Chen, D. Wu, J. Chu, Y. S. Kivshar, S. Xiao, and C.-W. Qiu, Observation of intrinsic chiral bound states in the continuum, Nature (London) **613**, 474 (2023).

[27] E. N. Bulgakov and D. N. Maksimov, Bound states in the continuum and polarization singularities in periodic arrays of dielectric rods, Phys. Rev. A **96**, 063833 (2017).

[28] H. M. Doeleman, F. Monticone, W. den Hollander, A. Alù, and A. F. Koenderink, Experimental observation of a polarization vortex at an optical bound state in the continuum, Nat. Photonics **12**, 397 (2018).

[29] W. Liu, B. Wang, Y. Zhang, J. Wang, M. Zhao, F. Guan, X. Liu, L. Shi, and J. Zi, Circularly polarized states spawning from bound states in the continuum, Phys. Rev. Lett. **123**, 116104 (2019).

[30] Z. Che, Y. Zhang, W. Liu, M. Zhao, J. Wang, W. Zhang, F. Guan, X. Liu, W. Liu, L. Shi, and J. Zi, Polarization singularities of photonic quasicrystals in momentum space, Phys. Rev. Lett. **127**, 043901 (2021).

[31] X. Yin, J. Jin, M. Soljačić, C. Peng, and B. Zhen, Observation of topologically enabled unidirectional guided resonances, Nature (London) **580**, 467 (2020).

[32] S.-G. Lee, S.-H. Kim, and C.-S. Kee, Bound states in the continuum (BIC) accompanied by avoided crossings in leaky-mode photonic lattices, Nanophotonics **9**, 4373 (2020).

[33] C. Zhao, G. Hu, Y. Chen, Q. Zhang, Y. Zhang, and C.-W. Qiu, Unidirectional bound states in the continuum in Weyl semimetal nanostructures, Photonics Res. **10**, 1828 (2022).

[34] I. Volkovskaya, L. Xu, L. Huang, A. I. Smirnov, A. E. Micoshnichenko, and D. Smirnova, Multipolar second-harmonic generation from high-Q quasi-BIC states in subwavelength resonators, Nanophotonics **9**, 3953 (2020).

[35] G. Zograf, K. Koshelev, A. Zalogina, V. Korolev, R. Hollinger, D.-Y. Choi, M. Zuerch, C. Spielmann, B. Luther-Davies, D. Kartashov, S. V. Makarov, S. S. Kruk, and Y. Kivshar, High-harmonic generation from resonant dielectric metasurfaces

empowered by bound states in the continuum, ACS Photonics **9**, 567 (2022).

[36] T. Liu, M. Qin, F. Wu, and S. Xiao, High-efficiency optical frequency mixing in an all-dielectric metasurface enabled by multiple bound states in the continuum, Phys. Rev. B **107**, 075441 (2023).

[37] X. Qi, J. Wu, F. Wu, M. Ren, Q. Wei, Y. Wang, H. Jiang, Y. Li, Z. Guo, Y. Yang, W. Zheng, Y. Sun, and H. Chen, Steerable merging bound states in the continuum on a quasi-flatband of photonic crystal slab without breaking symmetry, Photonics Res. **11**, 1262 (2023).

[38] T.-Y. Zeng, G.-D. Liu, L.-L. Wang, and Q. Lin, Light-matter interactions enhanced by quasi-bound states in the continuum in a graphene-dielectric metasurface, Opt. Express **29**, 40177 (2021).

[39] I. A. M. Al-ani, K. As'Ham, L. Huang, A. E. Miroshnichenko, W. Lei, and H. T. Hattori, Strong coupling of exciton and high-Q mode in all-perovskite metasurfaces, Adv. Opt. Mater. **10**, 2101120 (2022).

[40] S. Li, C. Zhou, T. Liu, and S. Xiao, Symmetry-protected bound states in the continuum supported by all-dielectric metasurfaces, Phys. Rev. A **100**, 063803 (2019).

[41] S. I. Azzam, V. M. Shalaev, A. Boltasseva, and A. V. Kildishev, Formation of bound states in the continuum in hybrid plasmonic-photonic systems, Phys. Rev. Lett. **121**, 253901 (2018).

[42] D. C. Marinica, A. G. Borisov, and S. V. Shabanov, Bound states in the continuum in photonics, Phys. Rev. Lett. **100**, 183902 (2008).

[43] W. Liu, Y. Li, H. Jiang, Z. Lai, and H. Chen, Controlling the spectral width in compound waveguide grating structures, Opt. Lett. **38**, 163 (2013).

[44] K. Sun, H. Jiang, D. A. Bykov, V. Van, U. Levy, Y. Cai, and Z. Han, 1D quasi-bound states in the continuum with large operation bandwidth in the $\omega \sim k$ space for nonlinear optical applications, Photonics Res. **10**, 1575 (2022).

[45] Y. Gao, J. Ge, S. Sun, and X. Shen, Dark modes governed by translational-symmetry-protected bound states in the continuum in symmetric dimer lattices, Results Phys. **43**, 106078 (2022).

[46] Y. H. Ko, K. J. Lee, F. A. Simlan, and R. Magnusson, Singular states of resonant nanophotonic lattices, Nanophotonics **12**, 263 (2023).

[47] M. Cotrufo, A. Cordaro, D. L. Sounas, A. Polman, and A. Alù, Passive bias-free non-reciprocal metasurfaces based on thermally nonlinear quasi-bound states in the continuum, Nat. Photonics **18**, 81 (2024).

[48] A. C. Overvig, S. Shrestha, and N. Yu, Dimerized high contrast gratings, Nanophotonics **7**, 1157 (2018).

[49] J. Wang, A. Chen, M. Zhao, W. Liu, Y. Zhang, X. Liu, L. Shi, and J. Zi, Observation of optical states below the light cone with compound lattices, OSA Continuum **2**, 1844 (2019).

[50] W. Wang, L. V. Besteiro, P. Yu, F. Lin, A. O. Govorov, H. Xu, and Z. Wang, Plasmonic hot-electron photodetection with quasi-bound states in the continuum and guided resonances, Nanophotonics **10**, 1911 (2021).

[51] T. Shi, Z.-L. Deng, Q.-A. Tu, Y. Cao, and X. Li, Displacement-mediated bound states in the continuum in all-dielectric superlattice metasurfaces, PhotoniX **2**, 7 (2021).

[52] W. Shi, J. Gu, X. Zhang, Q. Xu, J. Han, Q. Yang, L. Cong, and W. Zhang, Terahertz bound states in the continuum with incident angle robustness induced by a dual period metagrating, Photonics Res. **10**, 810 (2022).

[53] K. Sun, H. Wei, W. Chen, Y. Chen, Y. Cai, C.-W. Qiu, and Z. Han, Infinite-Q guided modes radiate in the continuum, Phys. Rev. B **107**, 115415 (2023).

[54] R. Jin, L. Huang, C. Zhou, J. Guo, Z. Fu, J. Chen, J. Wang, X. Li, F. Yu, J. Chen, Z. Zhao, X. Chen, W. Lu, and G. Li, Toroidal dipole BIC-driven highly robust perfect absorption with a graphene-loaded metasurface, Nano. Lett. **23**, 9105 (2023).

[55] F. Wu, J. Wu, Z. Guo, H. Jiang, Y. Sun, Y. Li, J. Ren, and H. Chen, Giant enhancement of the Goos-Hänchen shift assisted by quasibound states in the continuum, Phys. Rev. Appl. **12**, 014028 (2019).

[56] T. Ning, X. Li, Y. Zhao, L. Yin, Y. Huo, L. Zhao, and Q. Yue, Giant enhancement of harmonic generation in all-dielectric resonant waveguide gratings of quasi-bound states in the continuum, Opt. Express **28**, 34024 (2020).

[57] Z. Huang, M. Wang, Y. Li, J. Shang, K. Li, W. Qiu, J. Dong, H. Guan, Z. Chen, and H. Lu, Highly efficient second harmonic generation of thin film lithium niobate nanograting near bound states in the continuum, Nanotechnology **32**, 325207 (2021).

[58] Y. Ruan, Z.-D. Hu, J. Wang, L. Yu, and Y. Wang, Adjacent asymmetric tilt grating structure with strong resonance assisted by quasi-bound states in the continuum, IEEE Photonics J. **14**, 4655906 (2022).

[59] F. Wu, T. Liu, Y. Long, S. Xiao, and G. Chen, Giant photonic spin Hall effect empowered by polarization-dependent quasi-bound states in the continuum in compound grating waveguide structures, Phys. Rev. B **107**, 165428 (2023).

[60] X. Li, D. Liu, Y. Huo, Q. Yue, and T. Ning, Low-voltage electro-optic switching and modulation of second harmonic generation in lithium niobate resonant waveguide gratings assisted by quasi-BICs, Opt. Laser Technol. **160**, 109083 (2023).

[61] J. Liu, C. Chen, X. Li, J. Li, D. Dong, Y. Liu, and Y. Fu, Tunable dual quasi-bound states in the continuum and electromagnetically induced transparency enabled by the broken material symmetry in all-dielectric compound gratings, Opt. Express **31**, 4347 (2023).

[62] S. Zhang, M. Zong, Y. Liu, Z. Wu, J. Lv, and Z. Xu, Independent dual-band bound states in the continuum supported by double asymmetric periodic gratings in Germanium-based structure, Laser Photon. Rev. 2301206 (2023).

[63] S. Feng, T. Liu, W. Chen, F. Wu, and S. Xiao, Enhanced sum-frequency generation from etchless lithium niobate empowered by dual quasi-bound states in the continuum, Sci. China: Phys. Mech. Astron. **66**, 124214 (2023).

[64] Y. He, G. Guo, T. Feng, Y. Xu, and A. E. Miroshnichenko, Toroidal dipole bound states in the continuum, Phys. Rev. B **98**, 161112(R) (2018).

[65] A. S. Kupriiannov, K. L. Domina, V. V. Khardikov, A. B. Evlyukhin, and V. R. Tuz, Homogeneous enhancement of near-fields in all-dielectric metasurfaces with cluster-based unit cells, Opt. Lett. **45**, 1527 (2020).

[66] S. Xiao, M. Qin, J. Duan, F. Wu, and T. Liu, Polarization-controlled dynamically switchable high-harmonic generation

from all-dielectric metasurfaces governed by dual bound states in the continuum, Phys. Rev. B **105**, 195440 (2022).
[67] Y. Gao, L. Xu, and X. Shen, *Q*-factor mediated quasi-BIC resonances coupling in asymmetric dimer lattices, Opt. Express **30**, 46680 (2022).
[68] A. C. Overvig, S. C. Malek, M. J. Carter, S. Shrestha, and N. Yu, Selection rules for quasibound states in the continuum, Phys. Rev. B **102**, 035434 (2020).
[69] S. C. Malek, A. C. Overvig, S. Shrestha, and N. Yu, Active nonlocal metasurfaces, Nanophotonics **10**, 655 (2021).
[70] S. C. Malek, A. C. Overvig, A. Alù, and N. Yu, Multifunctional resonant wavefront-shaping meta-optics based on multilayer and multi-perturbation nonlocal metasurfaces, Light Sci. Appl. **11**, 246 (2022).
[71] S. Murai, D. R. Abujetas, L. Liu, G. W. Castellanos, J. A. Sánchez-Gil, K. Tanaka, and J. G. Rivas, Engineering bound states in the continuum at telecom wavelengths with non-Bravais lattices, Laser Photonics Rev. **16**, 2100661 (2022).
[72] P. Vaity, H. Gupta, A. Kala, S. D. Gupta, Y. S. Kivshar, V. R. Tuz, and V. G. Achanta, Polarization-independent quasibound states in the continuum, Adv. Photonics Res. **3**, 2100144 (2022).
[73] J. Fan, Z. Li, Z. Xue, H. Xing, D. Lu, G. Xu, J. Gu, J. Han, and L. Cong, Hybrid bound states in the continuum in terahertz metasurfaces, Opto-Electron. Sci. **2**, 230006 (2023).
[74] M. Zhou, S. You, L. Xu, M. Fan, J. Huang, W. Ma, M. Hu, S. Luo, M. Rahmani, Y. Cheng, L. Li, C. Zhou, L. Huang, and A. E. Miroshnichenko, Bound states in the continuum in all-dielectric metasurfaces with scaled lattice constants, Sci. China: Phys. Mech. Astron. **66**, 124212 (2023).
[75] A. Sadreev, Lattice distortion generates bound states in the continuum, Sci. China: Phys. Mech. Astron. **67**, 234231 (2024).
[76] S. Lv, H. Xu, W. Luo, F. Hu, and Y. Dang, Multipole interference and optical sensing based on the bound states in the continuum formed in dimer metasurfaces, Results Phys. **54**, 107088 (2023).
[77] W. Wang, Y. K. Srivastava, T. C. Tan, Z. Wang, and R. Singh, Brillouin zone folding driven bound states in the continuum, Nat. Commun. **14**, 2811 (2023).
[78] G. C. G. Berkhout, M. P. J. Lavery, J. Courtial, M. W. Beijersbergen, and M. J. Padgett, Efficient sorting of orbital angular momentum states of light, Phys. Rev. Lett. **105**, 153601 (2010).
[79] J. Ni, C. Huang, L.-M. Zhou, M. Gu, Q. Song, Y. Kivshar, and C.-W. Qiu, Multidimensional phase singularities in nanophotonics, Science **374**, eabj0039 (2021).
[80] V. G. Kravets, F. Schedin, R. Jalil, L. Britnell, R. V. Gorbachev, D. Ansell, B. Thackray, K. S. Novoselov, A. K. Geim, A. V. Kabashin, and A. N. Grigorenko, Singular phase nano-optics in plasmonic metamaterials for label-free single-molecule detection, Nat. Mater. **12**, 304 (2013).
[81] A. Berkhout and A. F. Koenderink, Perfect absorption and phase singularities in plasmon antenna array etalons, ACS Photonics **6**, 2917 (2019).
[82] M. Liu, W. Chen, G. Hu, S. Fan, D. N. Christodoulides, C. Zhao, and C.-W. Qiu, Spectral phase singularity and topological behavior in perfect absorption, Phys. Rev. B **107**, L241403 (2023).
[83] Y. Deng, C. Wu, C. Meng, S. I. Bozhenvolnyi, and F. Ding, Functional metasurface quarter-wave plates for simultaneous polarization conversion and beam steering, ACS Nano **15**, 18532 (2021).
[84] F. Wu, M. Chen, and S. Xiao, Wide-angle polarization selectivity based on anomalous defect mode in photonic crystal containing hyperbolic metamaterials, Opt. Lett. **47**, 2153 (2022).
[85] P. Hlubina, D. Ciprian, and J. Lunacek, Spectral interferometric technique to measure the ellipsometric phase of a thin-film structure, Opt. Lett. **34**, 2661 (2009).
[86] P. Hlubina, M. Lunackova, and D. Ciprian, Phase sensitive measurement of the wavelength dependence of the complex permittivity of a thin gold film using surface plasmon resonance, Opt. Mater. Express **9**, 992 (2019).
[87] K. V. Sreekanth, S. Sreejith, S. Han, A. Mishra, X. Chen, H. Sun, C. T. Lim, and R. Singh, Biosensing with the singular phase of an ultrathin metal-dielectric nanophotonic cavity, Nat. Commun. **9**, 369 (2018).
[88] X. Yue, T. Wang, R. Yan, L. Wang, H. Wang, Y. Wang, J. Zhang, and J. Wang, High-sensitivity refractive index sensing with the singular phase in normal incidence of an asymmetric Fabry-Perot cavity modulated by grating, Opt. Laser Technol. **157**, 108697 (2023).
[89] S.-G. Huang, K.-P. Chen, and S.-C. Jeng, Phase sensitive sensor on Tamm plasmon devices, Opt. Mater. Express **7**, 1267 (2017).
[90] Y. Tsurimaki, J. K. Tong, V. N. Boriskin, A. Semenov, M. I. Ayzatsky, Y. P. Machekhin, G. Chen, and S. V. Boriskina, Topological engineering of interfacial optical Tamm states for highly sensitive near-singular-phase optical detection, ACS Photonics **5**, 929 (2018).
[91] S. V. Boriskina and Y. Tsurimaki, Sensitive singular-phase optical detection without phase measurements with Tamm plasmons, J. Phys.: Condens. Matter **30**, 224003 (2018).
[92] A. Juneau-Fecteau and J. G. Fréchette, Tamm plasmon-polaritons in a metal coated porous silicon photonic crystal, Opt. Mater. Express **8**, 2774 (2018).
[93] N. K. Gupta, A. K. Tiwari, H. Wanare, and S. A. Ramakrishna, Near singular-phase optical biosensing with strongly coupled modes of a plasmonic-photonic trimer, J. Opt. **23**, 065003 (2021).
[94] Y. Li, T. Yang, S. Song, Z. Pang, G. Du, and S. Han, Phase properties of Bloch surface waves and their sensing applications, Appl. Phys. Lett. **103**, 041116 (2013).
[95] B. Kalas, K. Ferencz, A. Saftics, Z. Czipany, M. Fried, and P. Petrik, Bloch surface waves biosensing in the ultraviolet wavelength range—Bragg structure design for investigating protein adsorption by *in situ* Kretschmann-Raether ellipsometry, Appl. Surf. Sci. **536**, 147869 (2021).
[96] M. F. Al-Kuhaili, Optical properties of hafnium oxide thin films and their applications in energy-efficient windows, Opt. Mater. **27**, 383 (2004).
[97] E. Palik, *Handbook of Optical Constants of Solid I* (Academic Press, New York, 1985).
[98] T. Sang, S. Cai, and Z. Wang, Guided-mode resonance filter with an antireflective surface consisting of a buffer layer with refractive index equal to that of the grating, J. Mod. Opt. **58**, 1260 (2011).

[99] A. Yariv and P. Yeh, *Optical Waves in Crystals* (Wiley, New York, 1984).

[100] S. A. Dyakov, V. A. Semenenko, N. A. Gippius, and S. G. Tikhodeev, Magnetic field free circularly polarized thermal emission from a chiral metasurface, Phys. Rev. B **98**, 235416 (2018).

[101] S. A. Dyakov, M. V. Stepikhova, A. A. Bogdanov, A. V. Novikov, D. V. Yurasov, M. V. Shaleev, Z. F. Krasilnik, S. G. Tikhodeev, and N. A. Gippius, Photonic bound states in the continuum in Si structures with the self-assembled Ge nanoislands, Laser Photonics Rev. **15**, 2000242 (2021).

[102] M. G. Moharam, D. A. Pommet, E. B. Grann, and T. K. Gaylord, Stable implementation of the rigorous coupled-wave analysis for surface-relief gratings: Enhanced transmittance matrix approach, J. Opt. Soc. Am. A **12**, 1077 (1995).

[103] F. Li, Use of Fourier series in the analysis of discontinuous periodic structures, J. Opt. Soc. Am. A **13**, 1870 (1996).

[104] See Supplemental Material at http://link.aps.org/supplemental/10.1103/PhysRevB.109.085436 for eigenfrequencies and eigenmode profiles of momentum mismatch driven quasi-BICs and BIC; effects of height of waveguide layer on momentum mismatch driven BICs and ultrasensitive refractive index sensing; and ultrasensitive refractive index sensing enabled by a drastic ellipsometric phase change at visible wavelengths.

[105] Z. Liu, Y. Xu, Y. Lin, J. Xiang, T. Feng, Q. Cao, J. Li, S. Lan, and J. Liu, High-Q quasibound states in the continuum for nonlinear metasurfaces, Phys. Rev. Lett. **123**, 253901 (2019).

[106] K. V. Sreekanth, Y. Alapan, M. ElKabbash, E. Ilker, M. Hinczewski, U. A. Gurkan, A. De Luca, and G. Strangi, Extreme sensitivity biosensing platform based on hyperbolic metamaterials, Nat. Mater. **15**, 621 (2016).

[107] B. Moeinimaleki, K. Moeinimaleki, Z. Mardani, and S. Karamzadeh, Design and simulation of refractive index sensor based on suspended composite hybrid plasmonic waveguide for sensing mass density of polarizable hydrogen gas, J. Nanophotonics **17**, 036003 (2023).

[108] T. Xue, W. Liang, Y. Li, Y. Sun, Y. Xiang, Y. Zhang, Z. Dai, Y. Duo, L. Wu, K. Qi, B. N. Shivananju, L. Zhang, X. Cui, H. Zhang, and Q. Bao, Ultrasensitive detection of miRNA with an antimonene-based surface plasmon resonance sensor, Nat. Commun. **10**, 28 (2019).

[109] Y. Huang, H. P. Ho, S. K. Kong, and A. V. Kabashin, Phase-sensitive surface plasmon resonance biosensors: Methodology, instrumentation and applications, Ann. Phys. **524**, 637 (2012).

[110] F. Sohrabi, S. Saeidifard, and S. M. Hamidi, Plasmonic structures for phase-sensitivity ellipsometry biosensing: A review, Opt. Quantum Electron. **53**, 710 (2021).